

1

2

3     **Styles, Textural Evolution, and Sulfur Isotope Systematics of Cu-rich**  
4     **Sulfides from the Cambrian Whalesback Volcanogenic Massive Sulfide**  
5             **(VMS) Deposit, Central Newfoundland, Canada**

6

7

8     Jonathan Cloutier<sup>1\*</sup>, Stephen J. Piercey<sup>1</sup>, Graham Layne<sup>1</sup>, John Heslop<sup>2</sup>, Andrew Hussey<sup>2</sup>  
9     and Glenn Piercey<sup>3</sup>.

10

11

12     <sup>1</sup> Department of Earth Sciences, Memorial University of Newfoundland, 300 Prince  
13     Philip Drive, St. John's, NL, Canada, A1B 3X5.

14     <sup>2</sup> Thundermin Resources Inc., 133 Richmond Street West, Suite 300, Toronto, Ontario,  
15     Canada, M5H 2L3.

16     <sup>3</sup>Core Research Equipment and Instrument Training Network (CREAIT), Bruneau Centre  
17     for Research and Innovation, Memorial University of Newfoundland, P.O. Box 4200, St.  
18     John's, NL, A1C 5S7, Canada

19     \* Corresponding author: jonathanc@mun.ca

20

## Abstract

The Whalesback Cu-rich VMS deposit in the Newfoundland Appalachians is a highly deformed deposit found on a steep limb of a closed and boudinaged overturned fold. The deposit was intensely deformed at low temperature but medium pressure (>175 MPa) during the accretion of the composite Lushs Bight Oceanic Tract-Dashwoods terrane onto the Humber margin at ca. 480 Ma.

The ore mineralogy consists of chalcopyrite, pyrrhotite and pyrite with lesser sphalerite and trace Ag-, Bi- and Hg-tellurides. Four styles of sulfide mineralization are present: 1) disseminated (5%); 2) vein (50%); 3) breccia (25%); and 4) semi-massive to massive (20%). Independent of mineralization style, massive pyrite and pyrrhotite (and some chalcopyrite) are commonly parallel to main  $S_2$  schistosity in the deposit, whereas late chalcopyrite piercement veins occur at a high angle to  $S_2$ . The progressive increase in pressure and temperature produced a remobilization sequence wherein sphalerite was the first sulfide phase to cross the brittle-ductile boundary, followed by pyrrhotite and finally chalcopyrite. Maximum temperature was not high enough for the pyrite to cross the brittle-ductile boundary. Instead, pyrite grains were incorporated and transported by pyrrhotite and chalcopyrite during the ductile remobilization events, rounding and fracturing them. Remobilization of the sulfides occurred mainly by plastic flow, but some solution transport and re-precipitation is locally observed.

*In situ* secondary ion mass spectrometry (SIMS) sulfur isotopes geochemistry of sulfides yielded values of  $\delta^{34}\text{S}$  ranging from +2.7‰ to 4.7‰ for pyrite, +2.1‰ to 4.0‰ for pyrrhotite and +1.3‰ to 4.7‰ for chalcopyrite. Sulfur isotopic modeling suggests

43 that at least 60% of the sulfur was derived from leaching of igneous rocks (i.e., basalts),  
44 with the reminder derived from thermochemical sulfate reduction (TSR) of seawater  
45 sulfate during alteration of the basalts by seawater. At the deposit scale, sulfur isotopes  
46 retained their original signature and did not re-equilibrate during the secondary  
47 deformation and remobilization events.

## 48 **Introduction**

49 The Cu-rich Whalesback volcanic massive sulfide (VMS) deposit was discovered  
50 by the Betts Cove mining company in 1879 (Martin, 1983; Kean et al., 1995). In 1880,  
51 the property was sold to the Newfoundland Consolidated Copper Mining Company who  
52 dug numerous trenches and emplaced a 18m deep shaft in the hanging wall of the deposit,  
53 but no mineralization was encountered and exploration of the property stopped until  
54 mining rights were granted to the British Newfoundland Exploration Company  
55 (BRINEX) in 1957 (MacLean, 1947; Kean et al., 1995). Between 1960-1962, extensive  
56 exploration programs were jointly undertaken by BRINEX and the Anglo-American  
57 Corporation, successfully delineating a 2.7 million tonnes resource at 1.8% Cu. The  
58 Whalesback deposit entered production in 1963 and produce 3.8 million tonnes at 1% Cu  
59 over its 9 year mine life. In July 1972, the production ceased abruptly due a major cave-in  
60 breaching the surface and low Cu prices (Kean et al., 1995). More recently, an increase in  
61 the price of copper triggered a third exploration cycle at the Whalesback and adjacent  
62 Little Deer properties by Thundermin Resources Inc. To date, the Whalesback deposit  
63 has an indicated resource of 797,000 tonnes at 1.67% Cu (CIM/NI43-101; Brown, 2012)

64 The Whalesback deposit is a type example of an Appalachian stringer-dominated

65 Cyprus-type VMS deposit. Globally, Cyprus-type (also known as mafic-type) VMS  
66 deposits are commonly Cu-rich stratabound to stratiform, syngenetic deposits that form  
67 on or near the seafloor by precipitation from hydrothermal fluids at temperatures between  
68 200-350°C (e.g., Large, 1977; Franklin et al., 1981, 2005; Lydon, 1984, 1988;  
69 Hannington, 2014). The ore mineralogy of Cyprus-type commonly consists of pyrite,  
70 chalcopyrite, pyrrhotite and sphalerite with minor amounts of galena, tetrahedrite,  
71 tennantite, arsenopyrite, bornite, and magnetite (e.g., Large, 1977, 1992; Eldridge et al.,  
72 1983; Lydon, 1988; Ohmoto, 1996; Franklin et al., 2005). They often have metal zoning  
73 patterns that were driven by temperature-dependent metal solubility differences with low  
74 temperature Zn-(Pb) deposition followed by higher temperature Cu deposition; the latter  
75 often leading to zone refining of earlier formed Zn-(Pb) sulfides (Ohmoto, 1996). The  
76 Cu-rich sulfides in Cyprus-type deposits, and like those at Whalesback, generally  
77 precipitate from hotter fluids often adjacent or within the footwall feeder conduit or at the  
78 base of the sulfide mound), whereas Zn- and Pb-rich sulfides precipitate from cooler  
79 hydrothermal fluids at the top and outer margins of the deposits.

80 Cyprus-type deposits, like all VMS deposits generally form within extensional  
81 geodynamic regimes, with Cyprus-type systems generally forming at mid-ocean ridges,  
82 back-arc basins, and intra-oceanic arc rifts (e.g., Swinden, 1991a; Piercey, 2010, 2011;  
83 Hannington, 2014). In ancient environments, the extensional stage of tectonic activity is  
84 commonly followed by uplift, basin inversion, compressional deformation, and  
85 metamorphism of the sequence hosting the massive sulfide deposits often due to post-  
86 VMS formation accretionary tectonics (e.g., McClay, 1995; Nelson, 1997). During this  
87 accretionary activity, rheological differences between sulfides and more competent



110 by the Humber Zone and to the east by the Gander Zone (Williams, 1979; Williams et al.,  
111 1988; Hibbard et al., 2004). It represents the deformed vestiges of arcs, back arcs, and  
112 ophiolite complexes assembled during the closure of the Cambrian to Ordovician Iapetus  
113 Ocean (Fig. 1; Swinden et al., 1989; Swinden, 1991b; Kean et al., 1995; van Staal and  
114 Colman-Sadd, 1997; Evans and Kean, 2002; Rogers and van Staal, 2002; Rogers et al.,  
115 2006; van Staal, 2007; Zagorevski et al., 2010). The Dunnage Zone is divided into the  
116 western Notre Dame subzone, which formed near the Laurentian equatorial margin, and  
117 the eastern Exploits subzone, which formed on the edge of Gondwana and related  
118 microcontinents at mid- to high-southerly latitudes (e.g. Zagorevski et al., 2006; van Staal  
119 et al., 2007; Cocks and Torsvik, 2002). The Notre Dame subzone is subdivided into five  
120 zones which are, from oldest to youngest: 1) the Late Neoproterozoic–Cambrian ribbon-  
121 shaped Dashwoods microcontinent; 2) the 510-501 Ma mafic to ultramafic ophiolitic  
122 rocks of the Lushs Bight oceanic tract (LBOT); 3) the 489-477 Ma mafic to ultramafic  
123 ophiolitic rocks of the Baie Verte oceanic tract (BVOT); 4) the 488-453 Ma granodioritic  
124 to gabbroic Notre Dame magmatic arc; and 5) the 481-460 Ma ophiolite-arc-back arc  
125 tectonic collage of the Annieopsquotch accretionary tract (AAT) (Dunning and Krogh,  
126 1985; Elliot et al., 1991; Szybinski, 1995; Cawood et al., 1996; Swinden et al., 1997;  
127 Waldron and van Staal, 2001; Zagorevski et al., 2006; van Staal, 2007; van Staal et al.,  
128 2007; Skulski et al., 2010; van Staal and Barr, 2012).

129         The Whalesback VMS deposit occurs within the LBOT sequence. Obduction of  
130 the LBOT sequence onto the western margin of the Dashwoods microcontinent occurred  
131 during phase 1 of the Taconic orogeny, which was initiated between 500 and 493 Ma  
132 (Szybinski, 1995; Swinden et al., 1997; van Staal and Barr, 2012). The composite LBOT-

133 Dashwoods terrane was accreted onto the Humber margin at ca. 480 Ma during phase 2  
134 of the Taconic orogeny, resulting in the closure of the Taconic seaway and producing  
135 high-grade metamorphism and polyphase deformation in large parts of the Notre Dame  
136 subzone (van Staal, 2007; van Staal et al., 2007; van Staal and Barr, 2012). Collision of  
137 the Notre Dame subzone with the Exploits subzone occurred during phase 3 of the  
138 Taconic orogeny (455–450 Ma), initiating the collision of composite Laurentia with  
139 Ganderia, in which the peak of deformation occurred during the Salinic orogeny (445–  
140 423 Ma; Dunning et al., 1991; van Staal et al., 2003; van Staal, 2007; van Staal and Barr,  
141 2012; Zagorevski et al., 2010). Subsequent collision with the Avalon terrane during the  
142 Acadian orogeny (421–390 Ma), with the Meguma terrane during the Neocadian  
143 orogeny (ca. 395–340 Ma), and with Gondwana during the Alleghanian orogeny (ca. 340–  
144 260 Ma) lead to the formation of the Pangea supercontinent, ending ca. 250 m.y. of  
145 convergent tectonism (Hicks et al., 1999; Hatcher, 2002; Keppie et al., 2002; Reynolds et  
146 al., 2004; van Staal, 2005; van Staal et al., 2009; van Staal and Barr, 2012).

147

#### 148 *Geology of the Springdale Peninsula*

149       Following the stratigraphy established by Szybinski (1995), the LBOT is  
150 subdivided into three groups that are, from oldest to youngest: 1) the mafic Lushs Bight  
151 Group, 2) the dominantly mafic volcanic with minor felsic volcanic Western Arm Group,  
152 and 3) the bimodal volcanic Cutwell Group (Fig. 2; Marten, 1971a, 1971b; Kean, 1973;  
153 Kean and Strong, 1975; Kean et al., 1995; Szybinski, 1995). The Whalesback deposit  
154 occurs in the Lushs Bight Group (Figs. 2, 3). The Lushs Bight Group is 3–4 km thick and  
155 is predominantly composed of lower greenschist facies metamorphosed tholeiitic basalt

156 with local boninite and minor dioritic to gabbroic sheeted intrusions. Rare felsic  
157 pyroclastic rocks, jasper and magnetite-bearing chert are also present. The basalts occur  
158 as pillowed or massive flows, and can locally be variolitic. In most cases, the variolitic  
159 basalts are of boninitic affinity and have quartz-filled amygdules. Areas of VMS  
160 mineralization tend to be spatially associated with areas of abundant boninites and felsic  
161 pyroclastic rocks (Kean et al., 1995; Szybinski, 1995). The Lushs Bight Group is crosscut  
162 by several generations of intrusive rocks, which include gabbro, quartz dacite, plagioclase  
163 porphyry, hornblende porphyry, hornblende-plagioclase porphyry, and pyroxene  
164 porphyry (Kanehira and Bachinski, 1968; Szybinski, 1995). The Lushs Bight Group is  
165 characterized by strong epidote alteration of the basalts, with a general decrease in  
166 epidote abundance towards the stratigraphic top of the group, and by locally extensive  
167 quartz  $\pm$  carbonate veins (Kean et al., 1995).

168         The Lushs Bight Group was informally subdivided by Papezik and Fleming  
169 (1967) and Fleming (1970), on the basis of alteration, into a spilitic and chlorite altered  
170 “St. Patrick-type” and an epidote altered “Whalesback-type”. More recently, Szybinski  
171 (1995) subdivided the Lushs Bight Group into the basal Indian Head complex dominated  
172 by sheeted dikes and the overlying Little Bay Formation dominated by basalt.

173

#### 174 *Structural geology*

175         Szybinski (1995) recorded five stages of deformation in the Notre Dame Bay  
176 region. The first phase of deformation ( $D_1$ ) is a non-penetrative deformation linked with  
177 the mylonitization of pre-existing chlorite-rich syn-volcanic faults that were the feeder  
178 conduits to VMS mineralization, creating an  $S_1$  foliation. During  $D_1$ , these chlorite-rich



179 shear zones accommodated a component of dextral trans-current shearing (Szybinski,  
180 1995) related to dextral oblique convergence between the LBOT and Dashwoods micro-  
181 continent (Dewey, 2002), and was synchronous with phase 1 of the Taconic orogeny (van  
182 Staal, 2007; van Staal and Barr, 2012). The second phase of deformation ( $D_2$ ) produced a  
183 regional penetrative  $S_2$  foliation and tight to isoclinal upright folds with NE-NNE axial  
184 planes throughout the Lushs Bight Group. Szybinski (1995) concluded that  $D_2$  was  
185 synchronous with the emplacement of the Colchester and Coopers Cove plutons ( $465 \pm 2$   
186 Ma), and coincident with phase 2 of the Taconic orogeny. At Whalesback,  $D_2$  produced a  
187 steep  $S_2$  schistosity trending  $\sim 060^\circ N$  and dipping toward the southeast (Papezik, 1965;  
188 West, 1972). The third phase of deformation ( $D_3$ ) is also a significant regional event that  
189 produced many large NE-trending folds and numerous brittle-ductile NE-striking thrust  
190 faults related to the emplacement of an alpine-style nappe in the Notre Dame Bay region  
191 (Szybinski, 1995). At Whalesback,  $D_3$  resulted in the creation of an open fold with an  
192 axial trace trending  $\sim 025^\circ N$  and dipping steeply to the north, deforming the chlorite  
193 schists into a major dextral drag fold (West, 1972). The fourth phase of deformation ( $D_4$ )  
194 is locally evidenced in the Lushs Bight Group as ENE to SE plunging antiforms, folds  
195 and thrusts, and is not present near the Whalesback deposit.  $D_4$  reaches its maximum  
196 intensity in the vicinity of the Lobster Cove Fault, located approximately 10 km southeast  
197 of the study area. The fifth phase of deformation ( $D_5$ ) represents the third major regional  
198 event in the Lushs Bight Group and resulted in the creation of NE-SW trending folds  
199 verging to the NW, NNW trending high-angle thrust faults and foreland propagating  
200 duplexes of various sizes (Szybinski, 1995). At Whalesback, mafic dykes emplaced  
201 during  $D_1$  deformation are affected by NW directed high angle reverse faults (Szybinski,

202 1995).

203

204 *Geology of the Whalesback Deposit*

205 The Whalesback deposit is a Cu-rich (Cyprus-type) VMS deposit hosted in mafic  
206 volcanic rocks (Kanehira and Bachinski, 1968). It consists of veins, pods, and  
207 disseminated sulfides forming 0.3-15m wide mineralized lenses hosted within a 720m  
208 long and 120m wide highly chloritized shear zone that strikes 245°N and dips steeply  
209 towards the north (Figs. 3, 4). The Whalesback massive sulfide lenses are located in the  
210 central and hanging-wall portions of a chlorite shear zone that plunges southwest at about  
211 50° (Fig. 4; Kanehira and Bachinski, 1968). These lenses occur at the site of maximum  
212 deformation intensity within the chlorite shear zone(s), suggesting extensive  
213 remobilization during post VMS-formation deformation events. With increasing  
214 proximity to the main shear zone, pillow basalts from the Lushs Bight Group become  
215 increasingly sheared and elongated parallel to the shear planes, primary pyroxenes are  
216 replaced by secondary chlorite, epidote alteration decreases in intensity, and quartz  
217 aggregates replace albite laths (Kanehira and Bachinski, 1968). Barren, weakly altered,  
218 regionally metamorphosed, and deformed gabbro, quartz dacite, plagioclase porphyry,  
219 hornblende porphyry, hornblende-plagioclase porphyry, and pyroxene porphyry intrude  
220 the chlorite altered shear zone and the ore lenses (Kanehira and Bachinski, 1968).

221 The sulfide lenses consist of pyrite, chalcopyrite, pyrrhotite and sphalerite with  
222 minor mackinawite, pentlandite, magnetite, cubanite, galena, and ilmenite (Kanehira and  
223 Bachinski, 1968). The sulfides assemblages at the Whalesback deposit are spatially zoned  
224 with pyrrhotite and chalcopyrite being the dominant sulfides in the Eastern lenses,

225 whereas pyrite, sphalerite and chalcopyrite are the most abundant sulfides in the Western  
226 lenses (Fig. 4; West, 1972). Silicate alteration minerals associated with mineralization are  
227 predominantly chlorite and quartz with minor muscovite, carbonate, titanite, albite, and  
228 epidote (Kanehira and Bachinski, 1968). Alteration of the rocks surrounding the  
229 Whalesback deposit within the chlorite-rich shear zone is marked by depletion of Na and  
230 Ca and enrichment of Fe, S and K (Bachinski, 1977a), and is typical of VMS alteration  
231 systems (e.g. Franklin et al., 2005; Hannington, 2014 and references therein).

## 232 **Mineralization**

233 Detailed drill core logging and conventional optical petrography of mineralized  
234 intervals of 13 diamond drill cores acquired from the Western lenses and lower portion of  
235 the Eastern lenses, recently drilled by Thundermin Resources Inc., (Fig. 4) allowed the  
236 subdivision of the sulfide mineralization into four types: 1) disseminated; 2) veinlet; 3)  
237 breccia; and 4) semi-massive to massive. The sulfide minerals consist of chalcopyrite,  
238 pyrrhotite, pyrite and sphalerite, and coexist with silicate gangue minerals, which include  
239 chlorite (40-100%) with subordinate quartz (<50%), calcite (<40%), muscovite (<30%),  
240 epidote (<25%), feldspar (<20%) and titanite (<5%). Trace amounts (<0.01%) of 1-10 $\mu$ m  
241 long Ag, Bi and Hg tellurides were identified by scanning electron microscopy within the  
242 sulfide matrix.

243

### 244 *Textures and Distribution of Major Sulfide Phases*

245 *Western lenses.* Sulfides in the Western lenses consist of pyrite (~85%) with  
246 subordinate sphalerite (~10%)  $\pm$  chalcopyrite (~5%) hosted in highly chloritized basalts

247 (Fig. 5ab). Pyrite occurs as euhedral to subrounded grains and is spatially associated with  
248 quartz and sphalerite. Sphalerite occurs as small (<1 mm long) euhedral crystal  
249 aggregates that are interstitial to and infill fractures of pyrite grains, and commonly  
250 contains micro-inclusions of chalcopyrite, i.e., chalcopyrite disease (Barton and Bethke,  
251 1987). Greater abundances of sphalerite (up to 20%) are present in the semi-massive and  
252 massive pyrite intervals. Chalcopyrite occurs as anhedral grains with no visible individual  
253 grain boundaries, forming a matrix that crosscuts and fills fractures in pyrite and  
254 sphalerite. The chalcopyrite matrix locally contains 0.1-3 mm long subrounded to  
255 rounded pyrite grains.

256 *Eastern lenses.* Sulfides in the deeper portion of the Eastern lenses consist of  
257 chalcopyrite (~45%) with lesser pyrrhotite (~40%), pyrite (~15%), and trace sphalerite  
258 (<1%). Chalcopyrite and pyrrhotite have no observable internal grain boundaries and  
259 form a sulfide matrix that varies between pyrrhotite-rich and chalcopyrite-rich (Fig.  
260 5cdef). Chalcopyrite crosscuts and separates pyrrhotite-rich intervals into smaller  
261 aggregates, isolating them in its matrix (Figs. 5f, 6d, and 7ad). The chalcopyrite-  
262 pyrrhotite matrix contains angular to rounded, 0.1-3 mm long fractured pyrite grains and  
263 small aggregates of anhedral sphalerite that contain micro-inclusions of chalcopyrite, i.e.,  
264 chalcopyrite disease (Fig. 8a; Barton and Bethke, 1987). When sulfides are massive to  
265 semi-massive the chalcopyrite-pyrrhotite matrix fills fractures in pyrite and sphalerite  
266 (Figs. 7b, 8bc) and is locally intergrown with fibrous chlorite (Fig. 7b).

267

268 *Types of mineralization*

269            *Disseminated-type*. This mineralization type is dominated by pyrrhotite and pyrite  
270 with subordinate chalcopyrite and sphalerite, hosted by chlorite-rich basalt (Fig. 6a-c).  
271 Disseminated sulfides occur as discrete grains in proximity to vein-type mineralization  
272 (see below) and manifests itself as 1-3 mm long anhedral and asymmetrical grains that  
273 are weakly to strongly elongated parallel to sulfide veins. Disseminated sulfides are  
274 associated with >95% silicate matrix and account for ~5% of the total sulfide resource at  
275 the Whalesback deposit.

276            *Veinlet-type*. This mineralization type consists of chalcopyrite, pyrrhotite and  
277 pyrite veinlets that range from 1 to 10 mm in width. The veinlets have an anastomosing  
278 texture and commonly surround the angular to rounded fragments of the silicate gangue,  
279 usually dominated by quartz, and constitute 10-40% of the host rock (Fig. 6d-f).  
280 Pyrrhotite veinlets contain accessory rounded to subrounded pyrite and sphalerite, and are  
281 aligned parallel to  $S_2$ . In contrast, chalcopyrite veinlets are generally monomineralic and  
282 crosscut the pyrrhotite veinlets at a high angle. This type of mineralization accounts for  
283 ~50% of the total sulfide resource at the Whalesback deposit.

284            *Breccia-type*. This mineralization type consists of chalcopyrite, with minor  
285 pyrrhotite and pyrite. It contains 50-95% angular to subrounded dark chloritized basalt  
286 fragments within a 5-50% sulfide matrix (Fig. 6g-i). The breccia-type mineralization  
287 accounts for ~25% of the total sulfide resource at the Whalesback deposit.

288            *Semi-massive to massive sulfide*. This mineralization type consists of a mixture of  
289 chalcopyrite and subordinate pyrite and pyrrhotite in the Eastern lenses and of a mixture  
290 of pyrite and subordinate sphalerite and chalcopyrite in the Western lenses (Fig. 7a-f).  
291 Small, 1-5 mm long, subrounded to flattened (parallel to  $S_2$ ) fragments of silicate

292 minerals, mainly chlorite-altered wall rock, and constitute between 5 and 50% of the rock  
293 (Fig. 7ad). In areas with more intense deformation, the flattened fragments are  
294 heterogeneously distributed throughout the sulfide matrix, giving this type of  
295 mineralization a durchbewegung texture. Small 0.2-3 mm wide chalcopyrite veinlets  
296 commonly crosscut the semi-massive to massive sulfide assemblage (Fig. 7d). This type  
297 of mineralization accounts for ~20% of the total sulfide resource at the Whalesback  
298 deposit.

### 299 **Sulfur Isotopes**

300 One representative sample of massive sulfide from the Western lenses and five  
301 representative samples of massive sulfide (n=2), semi-massive sulfide (n=1), breccia  
302 (n=1) and veinlets (n=1) from the Eastern lenses (n=5) were chosen for *in situ* sulfur  
303 isotope analysis by secondary ion mass spectrometry (SIMS). Sample mounts were  
304 prepared from thin section off cuts by embedding ~1 cm x 1 cm pieces in epoxy in 1 inch  
305 diameter aluminum retaining rings. Samples were polished using standard lapidary  
306 procedures, and then sputter coated with 300 Å of Au to reduce charging under primary  
307 ion bombardment. All analyses were performed using a Cameca IMS 4f SIMS instrument  
308 at the MAF-IIC Microanalysis Facility at Memorial University.

309 The  $\delta^{34}\text{S}$  data was collected from pyrite, pyrrhotite, and chalcopyrite using the  
310 method described in Toman (2013) and Brueckner et al. (2014). In summary,  
311 determinations were performed by bombarding the sample with a primary ion microbeam  
312 of 600-850 picoamps (pA) of  $\text{Cs}^+$ , accelerated through a nominal 10 kiloelectron volt  
313 (keV) potential, and focused into a 5–15  $\mu\text{m}$  diameter spot on the sample. To exclude

314 exotic material in the polished surface from analysis, each spot was first pre-sputtered for  
315 100 s with a 25  $\mu\text{m}$  square raster applied to the beam. Negatively charged sputtered  
316 secondary ions were accelerated into the mass spectrometer of the instrument through a  
317 nominal potential of 4.5 keV. A combination of mass resolution (Mass Resolving Power  
318 approx. 2975) and energy filtering (sample offset -60 eV with a 40 eV energy window)  
319 were used to effectively eliminate isobaric interferences from  $^{16}\text{O}_2^-$  and  $^{33}\text{SH}^-$ . Signals for  
320  $^{32}\text{S}^-$ ,  $^{34}\text{S}^-$  and a background position at 31.67 Dalton (Da) were obtained by cyclical  
321 magnetic peak switching (typically 80 cycles were accumulated for each spot analysis),  
322 and detected using an electron multiplier in pulse counting mode. Standard counting  
323 times were: 0.5 s at the background position, 2.0 s on  $^{32}\text{S}^-$ , and 6.0 s on  $^{34}\text{S}^-$ . Waiting  
324 times of 0.25 s were inserted before each peak counting position to allow for magnet  
325 settling. All analyses are reported using the standard  $\delta$  notation in units of per mil (‰)  
326 relative to the international Vienna Canyon Diablo Troilite (VCDT) standard.

327 Internal precision on individual  $\delta^{34}\text{S}$  analysis is typically better than  $\pm 0.3\text{‰}$  ( $1\sigma$ ),  
328 whereas the overall reproducibility is typically better than  $\pm 0.5\text{‰}$  ( $1\sigma$ ). In house  
329 standards for pyrite (UL9B), pyrrhotite (PoW1) and chalcopyrite (Norilsk) were used to  
330 correct for instrumental mass fractionation for each specific mineral phase.

331

### 332 *Results*

333 Sulfide minerals from the Whalesback deposit display a relatively narrow range  
334 of sulfur isotope compositions. Measured  $\delta^{34}\text{S}$  of 18 pyrite samples range from +2.7 to  
335 +6.6 per mil with an average of +5.0 per mil; 7 pyrrhotite samples range from +2.1 per  
336 mil to +4.0 per mil with an average of +3.3 per mil; and 17 chalcopyrite samples range

337 from +1.3 to +4.7 per mil with an average of +2.9 per mil (Figs. 9a-f, 10, 11; Table 1).  
338 Within individual samples, the internal variations of  $\delta^{34}\text{S}$  in pyrrhotite and chalcopyrite  
339 are generally low (<0.6 per mil), with a maximum observed variation of 1.0 per mil (Fig.  
340 9a-f). Pyrite shows the greatest internal variations, and most of the  $\delta^{34}\text{S}$  range observed  
341 for Whalesback as a whole is present in one sample from the Eastern lenses (e.g., WB-  
342 12-106A\_561.05m, +4.5 to +6.4 per mil; Fig. 9c; Table 1). However, even for pyrite, the  
343 internal variation within individual grain is quite restricted in overall magnitude (3.5 to  
344 5.2 per mil; Fig 9c).

## 345 **Discussion**

### 346 *Morphology and Metal Zoning of the Whalesback Deposit*

347 The Whalesback deposit consists of a tightly folded and boudinaged deposit  
348 dominated by chalcopyrite and pyrrhotite in the Eastern lenses and by pyrite in the  
349 Western lenses (Fig. 4; Papezik, 1965; West, 1972; Szybinski, 1995). In most genetic and  
350 descriptive models for Cyprus-type VMS deposits, there is a well developed zonation of  
351 metals with chalcopyrite and pyrrhotite concentrated at the base and in the core of the  
352 deposits, and pyrite and sphalerite concentrated at the top and more distal parts of the  
353 deposit (Fig. 12a; e.g. Large, 1977; Franklin, 1981; Lydon, 1984, 1988; Ohmoto, 1996;  
354 Franklin et al., 2005; Hannington, 2014). The metal distribution at Whalesback suggests  
355 that the pyrite-rich Western lenses represent the top or distal parts of the Whalesback  
356 deposit, whereas the chalcopyrite-pyrrhotite-rich Eastern lenses represent the core and  
357 base of the deposit, in accordance with a younging direction towards west. Metal zoning  
358 projected above the present day surface implies that D<sub>2</sub> deformation produced a closed



359 overturned fold (Fig. 12c). Overturned folds at this location have not been previously  
360 documented and have implications for the longer-term exploration of the deposit.  
361 Furthermore, it confirms the Whalesback deposit has been highly deformed, folded and  
362 boudinaged during D<sub>2</sub> resulting in a closed overturned anticline (Fig. 12bc), and creating  
363 the characteristic durchbewegung deformation texture observed at hand specimen scale.

364

#### 365 *Sulfide textural evolution during deformation and remobilization*

366       Durchbewegung textured rocks are generally hosted within durchbewegung  
367 structures (Marshall and Gilligan, 1989), which form from the progression of folding and  
368 shearing related to the formation of tight to isoclinal folds. In these structures, the silicate  
369 layers surrounding the less competent sulfide layers become disrupted, detached and  
370 incorporated into the sulfides as they deform ductily. This process results in the creation  
371 of detached fold cores and boudins of varying geometry depending on competency  
372 contrast between the silicate and sulfide layers (Marshall and Gilligan, 1989). Relatively  
373 late piercement (or ductile) veins are commonly associated with the formation of  
374 durchbewegung structures. The veins range in size from a few centimeters to a few  
375 meters wide and generally form at high angle to the layer interface and fill in extensional  
376 planar fractures (Marshall and Gilligan, 1989).

377       At Whalesback, the majority of deformation and remobilization occurred during  
378 the D<sub>2</sub> deformation event, as most of the sulfide-rich zones are parallel to the main S<sub>2</sub>  
379 schistosity (Papezik, 1965; West, 1972; Szybinski, 1995). Remobilization and  
380 deformation of sphalerite, pyrrhotite, and chalcopyrite was due to ductile flow, whereas  
381 pyrite deformed brittly as demonstrated by its rounded habit and high degree of fracturing

382 (Figs. 7ab, 8a-d). Sphalerite, pyrrhotite, and chalcopyrite fill the fractures in pyrite,  
383 supporting their ductile remobilization. Moreover, pyrrhotite and chalcopyrite  
384 remobilization incorporated and transported pyrite grains, rounding and fracturing them  
385 (Figs. 8cd, 11def). Based on crosscutting relationships, sphalerite was the first sulfide  
386 phase to be remobilized followed by pyrrhotite and chalcopyrite, and the latter were  
387 followed by the formation of chalcopyrite veins (Fig. 8a-d). The sequence in which the  
388 sulfides crossed the brittle-ductile transition zone is indicative of low to medium pressure  
389 (>175 MPa) and low temperature deformation conditions, which were insufficient  
390 conditions for pyrite to deform ductily (Fig. 13; Marshall and Gilligan, 1987). These  
391 conditions are consistent with the lower greenschist grade metamorphism recorded  
392 elsewhere in the Lushs Bight Group (Kean et al., 1995).

393         The main transport mechanism of ductile sulfides at Whalesback, during peak  
394 metamorphism conditions, is interpreted to have been plastic flow, with minor solution  
395 transport and precipitation. Cox (1987) showed that the intergrowth of sulfides with  
396 fibrous phyllosilicates in low-grade metamorphic environments, like those observed at  
397 Whalesback, indicates that some material remobilization occurred by dissolution,  
398 solution transport and precipitation. However, since the intergrowth of fibrous chlorite  
399 with massive pyrrhotite and chalcopyrite is only observed locally (Figs. 7hi, 8b), it is  
400 assumed that plastic flow was likely the dominant transport mechanism.

401         The occurrence, and likely late remobilization, of chalcopyrite in high angle veins  
402 relative to  $S_2$  across the sulfide assemblages, is very common and expected in  
403 durchbewegung structures (Marshall and Gilligan, 1989), and suggests that the late  
404 chalcopyrite veins are a direct consequence of the structural evolution of the

405 durchbewegung structure hosting the Whalesback deposit. Close folding and boudinage  
406 of Cu-rich ore (Fig. 4) also support a structural evolution within a durchbewegung  
407 structure.

408

#### 409 *Influence of Deformation on $\delta^{34}\text{S}$ Distribution*

410 Only a few studies have investigated the effect of metamorphism on the primary  
411 sulfur isotopic composition of sulfide minerals in VMS deposits (e.g. Bachinski, 1977b;  
412 Craig and Vokes, 1993; Crowe, 1994; Cook and Hoefs, 1997; Wagner et al., 2004). Most  
413 of these studies were undertaken in areas affected by classic Barrovian-style  
414 metamorphism, i.e., where the temperature and the pressure gradually increase together,  
415 and all concluded, except Crowe (1994), that the original sulfur isotopic composition of  
416 individual sulfide phases was preserved during metamorphism. Bachinski (1977b)  
417 investigated the sulfur isotopic composition of VMS deposits within the Lushs Bight  
418 Group, including the former Whalesback mine, and reached a similar conclusion.

419 The  $\delta^{34}\text{S}$  values recorded from all sulfide phases during this study display a  
420 narrow range of +1.3 to +6.6 per mil and are heterogeneously distributed at the scale of  
421 the Whalesback deposit (Figs. 9a-f, 10, 11; Table 1). Pyrrhotite is the most consistent  
422 sulfide mineral with a range of only 1.9 per mil, followed by chalcopyrite with a range of  
423 3.4 per mil and pyrite with a range of 3.9 per mil. Equilibrium temperature derived from  
424 coexisting sulfides phases (chalcopyrite-pyrite, chalcopyrite-pyrrhotite, and pyrrhotite-  
425 pyrite) using Kajiwara and Krouse (1971) fractionation factors yield temperatures  
426 between 27 and 526°C (Fig. 14a-c) with one additional sample yielding a temperature of  
427 4605°C, above normal hydrothermal fluids and metamorphism temperature range. In

428 addition, one sample had a  $\Delta^{34}\text{S}_{\text{Py-Ccp}}$  of -0.6 that could not be solved using the  
429 equilibrium temperature equations of Kajiwara and Krouse (1971), indicating isotopic  
430 disequilibrium. Overall, most derived equilibrium temperatures are below the 200°C  
431 isotherm, which is lower than the typical Cu-rich VMS deposits formation temperature  
432 (250-350°C; Large, 1977; Franklin et al., 1981, 2005; Lydon, 1984, 1988; Hannington,  
433 2014). These low equilibrium temperatures can be due to a partial to complete re-  
434 equilibration of the sulfide phases at low temperature during the deformation and  
435 associated metamorphism (isotopic equilibrium), the product of primary precipitation of  
436 coexisting sulfide phases at different temperature yielding a low “apparent” equilibrium  
437 temperature (isotopic disequilibrium), or the result of isotopic heterogeneity of the  
438 mineralizing fluids through time induced by sulfur extraction from more than one source  
439 (isotopic disequilibrium).

440         Paragenetic relationships of sulfide phases at Whalesback suggest that the  
441 increase in pressure and temperature during D<sub>2</sub> produced a remobilization and  
442 deformation sequence wherein sphalerite crossed the brittle-ductile transition first,  
443 followed by pyrrhotite and by chalcopyrite. This remobilization may have lead to partial  
444 to complete re-equilibration of the sulfides. If complete isotopic equilibration was  
445 attained, each sulfide phases within the deformation zone should have a homogenous  
446 composition (i.e., all chalcopyrite should have similar  $\delta^{34}\text{S}$  values) and the derived  
447 equilibrium temperatures should be constant throughout the deposit, which is not the case  
448 at the Whalesback deposit (Figs. 10, 14a-c). Partial equilibration at hand sample scale is  
449 also unlikely as samples containing more than one sulfide pairs yield a wide range of  
450 equilibrium temperatures (Fig. 14a-c). It is therefore suggested that the sulfides are not in

451 isotopic equilibrium and at least partly retained their original isotopic composition, as  
452 previously proposed by Bachinski (1977b). However, given that the isotopic  
453 compositions of the ductile phases (pyrrhotite and chalcopyrite) are more homogeneous  
454 than the pyrite, it is suggested that some local homogenization may have occurred.

455         Using the fractionation factors of Ohmoto and Rye (1979), the maximum  
456 expected variation in  $\delta^{34}\text{S}$  between for a sulfide pair that precipitated from the same  
457 fluids, but at different temperatures (250-350°C), is 1.4 per mil for the pyrite-chalcopyrite  
458 pair, 0.3 per mil for the pyrrhotite-chalcopyrite pair, and 1.2 per mil the pyrite-pyrrhotite  
459 pair. These variations are not sufficient to explain the  $\delta^{34}\text{S}$  variation at Whalesback.  
460 Therefore, we suggest that variation in primary precipitation temperature of the  
461 coexisting sulfide phases is not important at the Whalesback deposit and that the  
462 provenance of sulfur is the main controlling factor on the  $\delta^{34}\text{S}$  distribution.

463

#### 464 *Origin of sulfur*

465         The sulfur in VMS deposits may originate from multiple sources, including: 1)  
466 sulfur derived from thermochemical sulfate reduction (TSR) of seawater sulfate via the  
467 partial reduction of oxidized seawater to isotopically lighter  $\text{H}_2\text{S}$  during seawater  
468 alteration of basement rocks. This process commonly results in sulfur in VMS sulfides  
469 that is ~17 to 25 per mil lighter than coexisting seawater sulfate (e.g., Sangster, 1968;  
470 Ohmoto and Rye, 1979; Ohmoto and Goldhaber, 1997; Huston, 1999; Shanks, 2001;  
471 Seal, 2000, 2006); seawater sulfate itself has varied greatly through geological time (+4  
472 to +34.5 per mil;  $\delta^{34}\text{S}_{\text{Cambrian}} = +34.5$  per mil; Claypool et al., 1980; Canfield et al., 2004;  
473 Kampschulte and Strauss, 2004; Paytan and Grey, 2012); 2) sulfur derived from anoxic

474 seawater with a sulfide isotopic composition 15 to 60 per mil lighter than sulfate derived  
475 from oxidized seawater (-25.5 to +19.5 per mil for Cambrian anoxic seawater; Goldhaber  
476 and Kaplan, 1975), and wherein the magnitude of the fractionation is related to  
477 sedimentation rates. Low sedimentation rates are associated with slower rate of sulfate  
478 reduction and larger fractionation, and high sedimentation rates are associated with faster  
479 rates of sulfate reduction and small fractionation. Sediments in anoxic environment are  
480 generally associated with elevated concentration of organic matter and sulfide minerals in  
481 which pyrite commonly display a framboidal texture (Goldhaber and Kaplan, 1975); 3)  
482 sulfide sulfur sourced by direct leaching from the basaltic rocks of the Lushs Bight Group  
483 underlying the mineralized stratigraphic horizons. In the case of submarine mafic  
484 volcanic hosted Cu-rich deposits, like Whalesback, the  $\delta^{34}\text{S}_{\text{Sulfides}}$  of basalt ranges from  
485 +0.3 to +0.7 per mil (Torssander, 1992); 4) magmatic sulfur with  $\delta^{34}\text{S}_{\text{Reservoir}} \approx +0 \pm 2$  per  
486 mil (Hoef, 2009). At temperatures above 300°C the dominant sulfur species is  $\text{SO}_2$ , but at  
487 lower temperatures the magmatic  $\text{SO}_2$  disproportionates rapidly to form  $\text{H}_2\text{S}$  and  $\text{H}_2\text{SO}_4$ .  
488 This latter reaction is accompanied by a large isotopic fractionation that produces  
489 negative  $\delta^{34}\text{S}_{\text{H}_2\text{S}}$  values often resulting in sulfides that have negative  $\delta^{34}\text{S}$  (Rye, 1993;  
490 Huston et al., 2011); and 5) bacteriogenic reduction of sulfate in marine or pore waters.  
491 Precipitation of sulfide by bacteria is associated with a strong fractionation, ranging from  
492 24 to 71 per mil and averaging  $51 \pm 10$  per mil, depending on the sulfate availability of  
493 the system (Ohmoto and Rye, 1979; Canfield and Teske, 1996; Ohmoto and Goldhaber,  
494 1997; Canfield, 2001; Seal, 2006). In the case of the Cambrian Whalesback deposit,  $\delta^{34}\text{S}$   
495 values ranging between -36.5 and +10.5 per mil with an average of  $-16.5 \pm 10$  per mil are  
496 expected for sulfide minerals derived from biogenic reduction of seawater sulfate during

497 the Cambrian (Kamprschulte and Strauss, 2004).

498         The absence of negative  $\delta^{34}\text{S}$  values, pyrite framboids, and the narrow positive  
499 range of  $\delta^{34}\text{S}$  obtained from the Whalesback deposit during this study (Table 1) suggest  
500 that biogenic sulfur input was insignificant. Furthermore, a significant component of  
501 magmatic sulfur is also highly unlikely, given these restricted positive  $\delta^{34}\text{S}$  values (i.e.,  
502 no evidence of sulfur disproportionation; Rye, 1993; Huston et al., 2011), and the  
503 absence of other features that are common to VMS deposits formed from magmatic fluid  
504 input, i.e. Au-Ag-enrichment, intermediate- to high-sulfidation ore mineral assemblages,  
505 and aluminous alteration assemblages (e.g., Sillitoe et al., 1996; Hannington et al., 1999;  
506 Dubé et al., 2007). Anoxic sulfur is also an unlikely sulfur source as carbonaceous and  
507 sulfur-rich sediments are rare in the vicinity of the Whaleback deposit. Moreover, the  
508 basalts of the Lushs Bight Group near the Whalesback deposit contain hematitized pillow  
509 lava with common to extensive magnetite-bearing red cherts (Kean et al., 1995),  
510 consistent with deposition in oxidized seawater.

511         To evaluate the relative roles of leaching from igneous host rocks and TSR,  
512 modeling was undertaken using the method described in Brueckner et al. (2014) using the  
513 equations outlined in Ohmoto and Rye (1979), Ohmoto and Goldhaber (1997), and Seal  
514 (2006). Thermochemical sulfate reduction (TSR) of seawater sulfate was modeled on the  
515 basis of three assumptions: 1) Cambrian seawater sulfate had a  $\delta^{34}\text{S} \approx +34.5$  per mil  
516 (Claypool et al., 1980; Canfield et al., 2004; Kamprschulte and Strauss, 2004; Paytan and  
517 Grey, 2012); 2) TSR occurred at  $\sim 300^\circ\text{C}$  (or higher), based on the observation of  
518 chalcopyrite-pyrrhotite assemblages in the sulfides; and 3) the system was open and was  
519 continuously replenished as the available heavy sulfate ( $\text{SO}_4$ ) was reduced to lighter  $\text{H}_2\text{S}$ ,

520 producing H<sub>2</sub>S with  $\delta^{34}\text{S}_{\text{H}_2\text{S}(300^\circ\text{C})} \approx +12.7$  per mil during TSR (i.e., assuming that  $f = 1$ ,  
521 where  $f$  is the fraction of SO<sub>4</sub> remaining in solution at site of reduction reaction). The  
522 fluid was then cooled from 300°C and various sulfide phases were precipitated, with most  
523 minerals precipitated at temperatures > 250-300°C given the chalcopyrite-rich  
524 assemblages at the Whalesback deposit. Figure 15 illustrates the sulfide isotopic  
525 composition as a function of cooling for the interpreted temperatures of deposition for  
526 sulfide solely derived from TSR. The model shows that TSR alone cannot generate the  
527  $\delta^{34}\text{S}$  range determined for the sulfide phases at the Whalesback deposit. Even at the  
528 modeled temperature of 250°C, TSR-derived sulfides would still have  $\delta^{34}\text{S}$  substantially  
529 heavier than the range observed at Whalesback. This implies that sulfur from leaching of  
530 igneous rocks must be an important contributor to the overall sulfur budget of the deposit.

531 Binary mixing proportions of sulfur sourced from mafic host rock leached H<sub>2</sub>S at  
532 300°C ( $\delta^{34}\text{S}_{\text{py}} \sim +1.2$  per mil,  $\delta^{34}\text{S}_{\text{po}} = +0.3$  per mil,  $\delta^{34}\text{S}_{\text{ccp}} = -0.2$  per mil) and sulfur  
533 derived from TSR at 300°C can be calculated using the following equation:

$$534 \quad \delta^{34}\text{S}_{\text{sample}} = X\delta^{34}\text{S}_{\text{TSR}} + (1-X)\delta^{34}\text{S}_{\text{leached}} \quad (1),$$

535 where  $\delta^{34}\text{S}$  is the measured sulfur isotopic signature of the sample,  $\delta^{34}\text{S}_{\text{TSR}} = \delta^{34}\text{S}$  derived  
536 from TSR calculation at 300°C for a given mineral phase,  $\delta^{34}\text{S}_{\text{leached}} = \delta^{34}\text{S}$  of igneous-  
537 derived sulfur in a given mineral phase at 300°C, and  $X$  is a proportionality factor that is  
538 1 when 100% of the sulfur is from TSR and 0 when there is 0% TSR (i.e., 100% leaching  
539 of igneous sulfur). The results show that sulfur derived from TSR at 300°C accounts for a  
540 maximum of ~40% of the sulfur budget of the Whalesback deposit, whereas between 60-  
541 90% has been derived from leaching from the surrounding footwall rocks (Fig. 16a-c).  
542 This result is expected given the high temperature nature of the mineralization at the



543 Whalesback deposit (i.e., Cu-rich assemblages) and the relatively restricted range of  
544 measured  $\delta^{34}\text{S}$  values, further arguing that leaching from nearby footwall rocks was the  
545 most important source for sulfur in the Whalesback deposit. Since the Lushs Bight Group  
546 is 3-4 km in thickness (Kean et al., 1995), there is no restriction for the depth at which the  
547 sulfur and metals present at Whalesback were extracted. However, given that copper  
548 solubility is low below 225°C and greatly increase with increasing temperature  
549 (Hannington et al., 2014), it is suggested that the sulfur and the metals were leached from  
550 the lower portion of the mafic Lushs Bight Group. This single mafic source for the  
551 extraction of the metals is also reflected in the simple mineralogy (chalcopyrite, pyrite,  
552 pyrrhotite, and subordinate sphalerite) encountered at the Whalesback deposit.

## 553 **Conclusions**

554 The Whalesback deposit is a Cu-rich VMS deposit hosted within a closed,  
555 boudinaged and overturned fold located within a durchbewegung structure. Intense  
556 deformation of the Whalesback deposit occurred at low temperature and medium  
557 pressure (>175 MPa) during the accretion of the LBOT-Dashwoods composite terrane  
558 onto the Humber margin at ca. 480 Ma ( $D_2$ ). The increase in pressure and temperature  
559 produced a remobilization sequence where sphalerite was the first sulfide phase to cross  
560 the brittle-ductile transition, followed by pyrrhotite and subsequently by chalcopyrite.  
561 The maximum metamorphic temperature was not high enough for pyrite to deform  
562 ductily. Instead, pyrite grains were incorporated and transported during the ductile  
563 remobilization of less competent sulfide phases (pyrrhotite and chalcopyrite). This led to  
564 the rounding and fracturing of the pyrite grains. Remobilization of sulfides occurred

565 primarily by plastic flow but some evidence of dissolution, solution transport and  
566 precipitation was observed locally.

567 Sulfur isotopes retained their original signatures and did not re-equilibrate during  
568 the remobilization events. The dominant source of sulfur was determined to be from  
569 sulfides leached from surrounding basalts, with a lesser component derived from  
570 thermochemical sulfate reduction of seawater sulfate during alteration of the basalts.

### 571 **Acknowledgements**

572 Financial and logistical support for this project was provided by Cornerstone Capital  
573 Resources, Thundermin Resources, an Natural Sciences and Engineering Research  
574 Council of Canada (NSERC) Collaborative Research and Development Grant to S.J.  
575 Piercey. Additional funding was provided by the NSERC-Altius Industrial Research  
576 Chair in Mineral Deposits (supported by NSERC, Altius Resources Inc., and the  
577 Research and Development Corporation of Newfoundland and Labrador) and an NSERC  
578 Discovery Grant to S.J. Piercey. The MAF-IIC SIMS Facility is supported by a Canada  
579 Foundation for Innovation Leader's Opportunity Fund (CFI-LOF) Grant to G.D. Layne.  
580 Jim Walker, Jan Peter, and David Lentz are thanked for their constructive criticisms and  
581 reviews of the manuscript.

582

## References

- 583
- 584 Bachinski, D.J., 1977a, Alteration associated with metamorphosed ophiolitic  
585 cupriferous iron sulfide deposits: Whalesback Mine, Notre Dame Bay,  
586 Newfoundland. *Mineralium Deposita*, v. 12, p. 48-63.
- 587 Bachinski, D.J., 1977b, Sulfur isotopic composition of ophiolitic cupriferous iron  
588 sulfide deposits, Notre Dame Bay, Newfoundland. *Economic Geology*, v.72, p.243-  
589 257.
- 590 Barrie, C. D., Boyle, A. P., Cook, N. J., and Prior, D. J., 2010a, Pyrite deformation  
591 textures in the massive sulfide ore deposits of the Norwegian Caledonides.  
592 *Tectonophysics*, v. 483, p. 269-286.
- 593 Barrie, C. D., Boyle, A. P., and Salter, M., 2010, How low can you go? - Extending  
594 downwards the limits of plastic deformation in pyrite. *Mineralogical Magazine*, v.  
595 73, p. 895-913.
- 596 Barton, P.B. Jr. and Bethke, P.M., 1987, Chalcopyrite disease in sphalerite: Pathology  
597 and epidemiology. *American Mineralogist*, v. 72, p. 451-467.
- 598 Brown, F., 2012, Whalesback mineral resource estimate. National Instrument 43-101  
599 report, 4p.
- 600 Brueckner, S.M., Piercey, S.J., Layne, G.D., Piercey, G. and Sylvester, P.J., 2014.  
601 Variations of sulfur isotope signatures in sulfides from the metamorphosed Cu(-Au)  
602 volcanogenic massive sulfide Ming deposit, Newfoundland Appalachians.  
603 *Mineralium Deposita*, DOI: 10.1007/s00126-014-0567-7. .
- 604 Canfield, D.E., 2001, Isotope fractionation by natural populations of sulfate-reducing

- 605 bacteria. *Geochimica et Cosmochimica Acta*, v. 65, no. 7, p. 1117-1124.
- 606 Canfield, D.E., 2004, The evolution of Earth surface sulfur reservoir. *American Journal*  
607 *of Science*, v. 304, p. 839-861.
- 608 Canfield, D.E., and Teske, A., 1996, Late Proterozoic rise in atmospheric oxygen  
609 concentration inferred from phylogenetic and sulfur-isotope studies. *Nature*, v. 382,  
610 p. 127-132.
- 611 Cawood, P.A., van Gool, J.A.M., and Dunning, G.R., 1996, Geological development of  
612 eastern Humber and western Dunnage zones: Corner Brook-Glover Island region,  
613 Newfoundland. *Canadian Journal of Earth Sciences*, v. 33, p. 182-198.
- 614 Claypool, G.E., Holser, W.T., Kaplan, I.R., Sakai, H., and Zar, I., 1980, The age curves  
615 of sulfur and oxygen isotopes in marine sulfate and their mutual interpretation.  
616 *Chemical Geology*, v. 28, p. 199-260.
- 617 Cocks, L.R.M., and Torsvik, T.H., 2002, Earth geography from 500 to 400 million years  
618 ago; a faunal and palaeomagnetic review. *Journal of the Geological Society of*  
619 *London*, v. 159, no. 6, p. 631-644.
- 620 Cook, N.J., and Hoefs, J., 1997, Sulphur isotope characteristics of metamorphosed Cu-  
621 (Zn) volcanogenic massive sulphide deposits in the Norwegian Caledonides.  
622 *Chemical Geology*, v. 135, p. 307-324.
- 623 Cox, S.F., 1987, Flow mechanisms in sulphide minerals. *Ore Geology Reviews*, v. 2, p.  
624 133-171.
- 625 Craig, J.R., and Vokes, F.M., 1993, The metamorphism of pyrite and pyritic ores: An  
626 overview. *Mineralogical Magazine*, v. 57, p. 3-18.
- 627 Crowe, D.E., 1994, Preservation of original hydrothermal  $\delta^{34}\text{S}$  values in greenschist to

628 upper amphibolite volcanogenic massive sulfide deposits. *Geology*, v. 22, p.873-  
629 876.

630 Dewey, J.F., 2002, Transtension in arcs and orogens. *International Geology Reviews*, v.  
631 44, p. 402-439.

632 Dubé, B., Gosselin, P. Mercier-Langevin, P., Hannington, M., and Galley, A., 2007,  
633 Gold-rich volcanogenic massive sulphide deposits. In: Goodfellow, W.D. (ed.),  
634 Mineral Deposits of Canada: A Synthesis of Major Deposit-Types, District  
635 Metallogeny, the Evolution of Geological Provinces, and Exploration Methods.  
636 Geological Association of Canada, Mineral Deposits Division, Special Publication  
637 No. 5, p. 75-94.

638 Dunning, G.R. and Krogh, T.E., 1985, Geochronology of ophiolites of the Newfoundland  
639 Appalachians. *Canadian Journal of Earth Sciences*, v. 22, p. 1659-1670.

640 Dunning, G.R., Swinden, H.S., Kean, B.F., Evans, D.T.W., and Jenner, G.A., 1991, A  
641 Cambrian island arc in Iapetus: Geochronology and geochemistry of the Lake  
642 Ambrose volcanic belt, Newfoundland Appalachians. *Geological Magazine*, v. 128,  
643 no. 1, p. 1-17.

644 Eldridge, C.S., Barton, P.B. Jr., and Ohmoto, H., 1983, Mineral textures and their bearing  
645 on formation of the Kuroko orebodies. *Economic Geology*, Monograph 5, p. 241-  
646 281.

647 Elliott, C.G., Dunning, G.R., and Williams, P.F., 1991, New constraints on the timing of  
648 deformation in eastern Notre Dame Bay, Newfoundland, from U/Pb zircon ages of  
649 felsic intrusions. *Geological Society of America Bulletin*, v. 103, p. 125-135.

650 Evans, D.T.W., and Kean, B.F., 2002, The Victoria Lake Supergroup, Central

651 Newfoundland - Its definition, setting and volcanogenic massive sulphide  
652 mineralization. Newfoundland Department of Mines and Energy, Geological  
653 Survey Open-File NFLD 2790, 68p.

654 Fleming, J.M., 1970, Petrology of the volcanic rocks of the Whalesback area,  
655 Springdale Peninsula, Newfoundland. MSc. thesis, Memorial University of  
656 Newfoundland, 107p.

657 Franklin, J. M., Gibson, H. L., Galley, A. G., and Jonasson, I. R., 2005, Volcanogenic  
658 massive sulfide deposits. In Hedenquist, J. W., Thompson, J. F. H., Goldfarb, R. J.,  
659 and Richards, J. P., (eds.), Economic Geology 100th Anniversary Volume. Society  
660 of Economic Geologists, p. 523-560.

661 Franklin, J.M., Lydon, J.W., and Sangster, D.F., 1981, Volcanic-associated massive  
662 sulfide deposits. In: Skinner, B.J. (ed.), 75th Anniversary Volume of Economic  
663 Geology. Lancaster, p. 485-627.

664 Hannington, M.D., 2014, Volcanogenic massive sulfide deposits, In: Holland, H.D., and  
665 Turekian, K.K (eds.), Treatise on Geochemistry (Second Edition), Elsevier, Oxford,  
666 p. 463-488.

667 Hannington, M.D., Poulsen, K.H., Thompson, J.F.H., and Sillitoe, R.H., 1999,  
668 Volcanogenic gold in the massive sulfide environment. Reviews in Economic  
669 Geology, v. 8, p. 319-350.

670 Hatcher, R.D., Jr., 2002, Alleghenian (Appalachian) orogeny, a product of zipper  
671 tectonics: Rotational transpressive continent-continent collision and closing of  
672 ancient oceans along irregular margins. In: Martinez, J.R. (ed.), Catalan, R.D.,  
673 Hatcher Jr., R., Arenas, R., and Diaz Garcia F., Variscan-Appalachian Dynamics:

674 the Building of the late Paleozoic Basement. Geological Society of America,  
675 Special Paper 364, p. 199-208.

676 Hibbard, J., van Staal, C., Rankin, D., and Williams, H., 2004, Lithotectonic map of the  
677 Appalachian Orogen, Canada-United States of America. Geological Survey of  
678 Canada, Map 2096A, scale 1:500,000.

679 Hicks, R.J., Jamieson, R.A., and Reynolds, P., 1999, Detrital and metamorphic  $^{40}\text{Ar}/^{39}\text{Ar}$   
680 ages from muscovite and whole-rock samples, Meguma Supergroup, southern Nova  
681 Scotia. Canadian Journal of Earth Sciences, v. 36, p. 23-32.

682 Hoef, J., 2009, Stable isotope geochemistry. 6<sup>th</sup> edition. Springer-Verlag. 286p.

683 Huston, D.L., 1999, Stable isotopes and their significance for understanding the genesis  
684 of volcanic-hosted massive sulfide deposits - A review. In Barrie, C.T., and  
685 Hannington, M.D. (eds.), Volcanic-associated massive sulfide deposits - Processes  
686 and examples in modern and ancient settings. Society of Economic Geologists  
687 Reviews in Economic Geology, v. 8, p. 261–295.

688 Huston, D.L., Relvas, J.M.R.S., Gemmel, J.B., and Driberg, S., 2011, The role of  
689 granites in volcanic-hosted massive sulphide ore-forming systems: An assessment  
690 of magmatic-hydrothermal contributions. Mineralium Deposita, v. 46, p. 473-507.

691 Kajiwarra, Y., and Krouse, H.R., 1971, Sulfur isotope partitioning in metallic sulphide  
692 systems. Canadian Journal of Earth Sciences, v. 8, p. 1397-1408.

693 Kampschulte, A., and Strauss, H., 2004, The sulfur isotopic evolution of Phanerozoic  
694 seawater based on the analysis of structurally substituted sulfate in carbonates.  
695 Chemical Geology, v. 204, p. 255-286.

696 Kanehira, K. and Bachinski, D.J., 1968, Mineralogy and textural relationships of ores

697 from the Whalesback Mine, northeast Newfoundland. Canadian Journal of Earth  
698 Sciences, v. 5, p. 1387-1395.

699 Kean, B.F., 1973, Stratigraphy, petrology and geochemistry of volcanic rocks of Long  
700 Island, Newfoundland. MSc. Thesis, Memorial University of Newfoundland, 155p.

701 Kean, B.F., and Strong, D.F., 1975, Geochemical evolution of an Ordovician island-arc  
702 of central Newfoundland Appalachians. American Journal of Science, v. 275, p. 97-  
703 118.

704 Kean, B.A., Evans, D.T.W., and Jenner, G.A., 1995, Geology and mineralization of the  
705 Lushs Bight Group. Newfoundland Department of Natural Resources, Report 95-2,  
706 204p.

707 Keppie, D.F., Keppie, J.D., and Murphy J.B., 2002, Saddle reef auriferous veins in a  
708 conical fold termination (Oldham anticline, Meguma terrane, Nova Scotia,  
709 Canada): Reconciliation of structural and age data. Canadian Journal of Earth  
710 Sciences, v. 39, p. 53-63.

711 Large, R.R., 1977, Chemical evolution and zonation of massive sulfide deposits in  
712 volcanic terrains. Economic Geology, v. 72, p. 549-572.

713 Large, R.R., 1992, Australian volcanic-hosted massive sulfide deposits: Features, styles,  
714 and genetic models. Economic Geology, v. 87, p. 471-510.

715 Lydon, J.W., 1984, Volcanogenic massive sulphide deposits Part I: A descriptive model.  
716 Geoscience Canada, v. 11, p. 195-202.

717 Lydon, J.W., 1988, Volcanogenic massive sulphide deposits Part 2: Genetic models.  
718 Geoscience Canada, v. 15, p. 43-65.

719 Marshall, B., and Gilligan, L.B., 1987, An introduction to remobilization: Information



720 from ore-body geometry and experimental considerations. *Ore Geology Reviews*,  
721 v. 2, p. 87-131.

722 Marshall, B., and Gilligan, L.B., 1989, Durchbewegung structure, piercement cusps, and  
723 piercement veins in massive sulfide deposits: Formation and interpretation.  
724 *Economic Geology*, v. 84, p. 2311-2319.

725 Marshall, B., and Gilligan, L.B., 1993, Remobilization, syn-tectonic processes and  
726 massive sulphide deposits. *Ore Geology Reviews*, v. 8, p. 39-64.

727 Marten, B.E., 1971a, The Geology of the Western Arm Group, Green Bay,  
728 Newfoundland. MSc. Thesis, Memorial University of Newfoundland, 72p.

729 Marten, B.E., 1971b, Stratigraphy of volcanic rocks in the Western Arm area of the  
730 Central Newfoundland Appalachians. *The Geological Association of Canada*  
731 *Proceedings*, v. 24, p. 73-84.

732 Martin, W., 1983, Once Upon a Mine: Story of Pre-Confederation Mines on the Island  
733 of Newfoundland. *Canadian Institute of Mining and Metallurgy, Special Volume*  
734 26, 98p.

735 MacLean, H.J., 1947, Geology and mineral deposits of the Little Bay area, *Geological*  
736 *Survey of Newfoundland, Bulletin 22*, 36p.

737 McClay, K.R., 1995, The geometries and kinematics of inverted fault systems: a review  
738 of analogue model studies. In: Buchanan, J.G. and Buchanan, P.G. (eds.), *Basin*  
739 *inversion. Geological Society Special Publication*, v. 88, p. 97-118.

740 Nelson, J., 1997, The quiet counter-revolution: Structural control of syngenetic deposits.  
741 *Geoscience Canada*, v. 24, no. 2, p. 91-98.

742 Ohmoto, H., and Rye, R.O., 1979, Isotopes of sulfur and carbon. In: Barnes, H.L. (ed.),

743           Geochemistry of hydrothermal ore deposits, 2nd ed., New York, Wiley, p. 509-567.

744   Ohmoto, H., 1996, Formation of volcanogenic massive sulfide deposits: The Kuroko  
745           perspective. *Ore Geology Reviews*, v. 10, p. 135-177.

746   Ohmoto, H., and Goldhaber, M.B., 1997, Sulfur and carbon isotopes. In: Barnes, H.L.  
747           (ed.), *Geochemistry of hydrothermal ore deposits*, 3rd ed., New York, John Wiley  
748           & Sons, p. 517-611.

749   Papezik, V.S., 1965, Report on the geology of the Whalesback southeast area in the Halls  
750           Bay area. British Newfoundland Exploration limited, unpublished report.

751   Papezik, V .S., and Fleming J.M., 1967, Basic volcanic rocks of the Whalesback area,  
752           Newfoundland. Geological Survey of Canada, Special Paper 4, p. 181-192.

753   Paytan, A., and Gray, E.T., 2012, Sulfur isotope stratigraphy. In: Gradstein, F.M., Ogg,  
754           J.G. (ed.) and Schmitz, M. *The geologic timescale 2012*. Amsterdam, Elsevier, p.  
755           167-180.

756   Piercey, S.J., 2010, An overview of petrochemistry in the regional exploration for  
757           volcanogenic massive sulphide (VMS) deposits. *Geochemistry: Exploration,*  
758           *Environment, Analysis*, v. 10, p. 1-18.

759   Piercey, S.J., 2011, The setting, style and role of magmatism in the formation of  
760           volcanogenic massive sulfide deposits. *Mineralium Deposita*, v. 46, p. 449-471.

761   Reynolds, P.H., Barr, S.M., White, C.E., and Ténière, P.J., 2004,  $^{40}\text{Ar}/^{39}\text{Ar}$  dating in the  
762           Lochaber-Mulgrave area, northern mainland Nova Scotia: Implications for timing  
763           of regional metamorphism and sediment provenance in the Late Devonian-Early  
764           Carboniferous Horton Group. *Canadian Journal of Earth Sciences*, v. 41, p. 987-  
765           996.

766 Rogers, N., and van Staal, C. R., 2002, Toward a Victoria Lake Supergroup: A  
767 provisional stratigraphic revision of the Red Indian to Victoria Lakes area, Central  
768 Newfoundland. Newfoundland Department of Mines and Energy, Geological  
769 Survey, Current Research, Report 02-1, p. 185-195.

770 Rogers, N., van Staal, C. R., McNicoll, V., Pollock, J., Zagorevski, A., and Whalen, J.,  
771 2006, Neoproterozoic and Cambrian arc magmatism along the eastern margin of  
772 the Victoria Lake Supergroup: A remnant of Ganderian basement in central  
773 Newfoundland? *Precambrian Research*, v. 147, p. 320-341.

774 Rye, R.O., 1993, The evolution of magmatic fluids in the epithermal environment: The  
775 stable isotope perspective. *Economic Geology*, v. 88, p. 733-753.

776 Sangster, D. R., 1968, Relative sulphur isotope abundances of ancient seas and strata-  
777 bound sulphide deposits. *Proceedings of the Geological Association of Canada*, v.  
778 19, p. 79-91.

779 Seal II, R.R., 2006, Sulphur isotope geochemistry of sulfide minerals. *Reviews in*  
780 *Mineralogy and Geochemistry*, v. 61, p. 633-677.

781 Seal II, R.R., Rye, R.O. and, Alpers, C.N., 2000, Stable isotope systematics of sulfate  
782 minerals. *Reviews in Mineralogy and Geochemistry*, v. 40, p. 541-602.

783 Shanks III, W.C., 2001, Stable isotopes in seafloor hydrothermal systems: Vent fluids,  
784 hydrothermal deposits, hydrothermal alteration, and microbial processes. In: Valley  
785 JW, and Cole, D.R. (ed.), *Stable isotope geochemistry. Reviews in Mineralogy and*  
786 *Geochemistry*, v. 43, p. 469-525.

787 Sillitoe, R.H., Hannington, M.D., and Thompson, J.F., 1996, High sulfidation deposits in  
788 the volcanogenic massive sulfide environment. *Economic Geology*, v. 91, p. 204-

789           212.

790 Skulski, T., Castonguay, S., McNicoll, V., van Staal, C.R., Kidd, W., Rogers, N., Morris,  
791 W., Ugalde, H., Slavinski, H., Spicer, W., Moussalam, Y., and Kerr, I., 2010,  
792 Tectonostratigraphy of the Baie Verte oceanic tract and its ophilitic cover sequence  
793 on the Baie Verte peninsula. Newfoundland and Labrador Department of Natural  
794 Resources. Geological Survey, Current Research, Report 10-1, p. 315-335.

795 Swinden, H.S., Jenner, G.A., Kean, B.F., and Evans, D.T.W., 1989, Volcanic rock  
796 geochemistry as a guide for massive sulphide exploration in Central Newfoundland.  
797 Government of Newfoundland and Labrador, Department of Mines and Energy,  
798 Mineral Development Division, Report of Activities 89-1, p. 201-219.

799 Swinden, H.S., 1991a, Paleotectonic settings of volcanogenic massive sulphide deposits  
800 in the Dunnage Zone, Newfoundland Appalachians. Canadian Institute of Mining  
801 and Metallurgy Bulletin, v. 84, no. 946, p. 59-89.

802 Swinden, H.S., 1991b, Regional geology and metallogeny of Central Newfoundland.  
803 Geological Survey of Canada, Open-File Report 2156, p. 1-27.

804 Swinden, H.S., Jenner, G.A., and Szybinski, Z.A., 1997, Magmatic and tectonic evolution  
805 of the Cambrian-Ordovician Laurentian margin of Iapetus: Geochemical and  
806 isotopic constraints from the Notre Dame subzone, Newfoundland. In: Sinha, A.K.  
807 (ed.), Whalen J.B., and Hogan J.P., The Nature of Magmatism in the Appalachian  
808 Orogen. Geological Society of America, Memoir 191, p. 367-395.

809 Szybinski, Z.A., 1995, Paleotectonic and structural setting of the western Notre Dame  
810 Bay area, Newfoundland Appalachians. Ph.D. thesis, Memorial University of  
811 Newfoundland. 481p.

812 Toman, H.C, 2013, Geology and Metallogeny of north-central Newfoundland and the  
813 Little Deer VMS deposit, Thesis M.Sc. Memorial University of Newfoundland  
814 2013, 184pp.

815 Torssander, P., 1992, Sulfur isotope ratios of leg 126 igneous rocks. In: Taylor, B.,  
816 FujioKa, K. et al., Proceedings of the Ocean Drilling Program, Scientific Results, v.  
817 126, p. 449-453.

818 van Staal, C.R., 2005, The Northern Appalachians. In: Selley, R.C., Cocks, L.R.M., and  
819 Plimer, I.R. (eds.), Encyclopedia of Geology. Oxford, Elsevier, v. 4, p. 81-91.

820 van Staal, C.R., 2007, Pre-Carboniferous metallogeny of the Canadian Appalachians. In:  
821 Goodfellow, W.D. (ed.), Mineral Deposits of Canada: A Synthesis of Major  
822 Deposit Types, District Metallogeny, the Evolution of Geological Provinces, and  
823 Exploration Methods. Mineral Deposits Division, Geological Association of  
824 Canada, Special Publication 5, p. 793-818.

825 van Staal, C.R. and Barr, S.M., 2012, Lithospheric architecture and tectonic evolution of  
826 the Canadian Appalachians and associated Atlantic margin. In: Percival, J.A.,  
827 Cook, F.A., and Clowes, .R.M. (eds.), Tectonic Styles in Canada: the  
828 LITHOPROBE Perspective. Geological Association of Canada, Special Paper 49,  
829 p. 41-98.

830 van Staal, C.R., and Colman-Sadd, S.P., 1997, The central Mobile Belt of the Northern  
831 Appalachians. Oxford Monographs on Geology and Geophysics, v. 35, p. 747-760.

832 van Staal, C.R., Whalen, J.B., McNicoll, V.J., Pehrsson, S.J., Lissenberg, C.J.,  
833 Zagorevski, A., van Breemen, O., and Jenner, G.A., 2007, The Notre Dame arc and  
834 the Taconic Orogeny in Newfoundland. In: Hatcher, J., Carlson Jr., M.P., McBride,

835 J. H., and Martínez Catalán, J.R. (eds.), 4-D Framework of Continental Crust.  
836 Geological Society of America, Memoir 200, p. 511-552.

837 van Staal, C.R., Whalen, J.B., Valverde-Vaquero, P., Zagorevski, A., and Rogers, N.,  
838 2009, Pre-Carboniferous, episodic accretion-related, orogenesis along the  
839 Laurentian margin of the northern Appalachians. In: Murphy, J.B., Keppie, J.D.,  
840 and Hynes, A.J. (eds.). Ancient Orogens and Modern Analogues. Geological  
841 Society London, Special Publication 327, p. 271-316.

842 van Staal, C.R., Wilson, R.A., Rogers, N., Fyffe, L.R., Langton, J.P., McCutcheon, S.R.,  
843 McNicoll, V., and Ravenhurst, C.E., 2003, Geology and tectonic history of the  
844 Bathurst Supergroup and its relationships to coeval rocks in southwestern New  
845 Brunswick and adjacent Maine – a synthesis. In: Goodfellow, W.D., McCutcheon,  
846 S.R., and Peter, J.M. (eds.), Massive Sulfide Deposits of the Bathurst Mining  
847 Camp, New Brunswick, and northern Maine. Economic Geology Monograph, v.  
848 11, p. 37-60.

849 Vokes, F.M., 1969, A review of the metamorphism of sulphide deposits. Earth Science  
850 Reviews, v. 5, p. 99-143.

851 Wagner, T., Boyce, A.J., Jonsson, E., and Fallick, A.E., 2004, Laser microprobe sulphur  
852 isotope analysis of arsenopyrite: Experimental calibration and application to the  
853 Boliden Au-Cu-As massive sulphide deposit. Ore Geology Reviews, v. 25, p. 311-  
854 325.

855 Waldron, J.W.F., and van Staal, C.R., 2001, Taconic Orogeny and the accretion of the  
856 Dashwoods block: a peri-Laurentian microcontinent in the Iapetus Ocean. Geology,  
857 v. 29, p. 811-814.

858 West, J.M.,1972, Structure and ore-genesis, Little Deer deposit, Whalesback Mines,  
859 Springdale, Newfoundland. MSc. thesis, Queen's University, 71p.

860 Williams, H., 1979, Appalachian Orogen in Canada. Canadian Journal of Earth Sciences,  
861 v.16, p. 792-807.

862 Williams, H., Colman-Sadd, S.P., and Swinden, H.S., 1988, Tectonostratigraphic  
863 subdivisions of Central Newfoundland. Geological Survey of Canada, Current  
864 Research, Part B, Paper 88-1B, 9p.

865 Zagorevski, A., Rogers, N., van Staal, C.R., McNicoll, V., Lissenberg, C.J., and  
866 Valverde-Vaquero, P., 2006, Lower to Middle Ordovician evolution of peri-  
867 Laurentian arc and back-arc complexes in the Iapetus: constraints from the  
868 Annieopsquotch Accretionary Tract, Central Newfoundland. Geological Society of  
869 America Bulletin, v. 118, p. 324-362.

870 Zagorevski, A., van Staal, C.R., Rogers, N., McNicholl, V., Dunning, G.R. and Pollock,  
871 J.C., 2010, Middle Cambrian to Ordovician arc-back arc development on the  
872 leading edge of Ganderia, Newfoundland Appalachians. In: Tollo, R.P.,  
873 Batholomew, M.J., Hibbard, J.P., and Karabinos, P.M. (eds.), From Rodinia to  
874 Pangea: The Lithotectonic Record of the Appalachian Region. Geological Society  
875 of America, Memoir 206, p. 367-396.

876

## List of Figures

877

878 Figure 1. Simplified geological map of the Newfoundland Appalachians with  
879 tectonostratigraphic zones (modified from van Staal, 2007, and van Staal and Barr, 2012).

880 Abbreviations: BBL = Baie Verte Brompton Line; DBL = Dog Bay Line; DF = Dover  
881 Fault; GBF = Green Bay Fault; LCF = Lobster Cove Fault; LRF = Lloyds River Fault;  
882 RIL = Red Indian Line.

883

884 ; LR = Long Range; LRF = Lloyds River Fault; PP = Pipestone Pond Complex; RIL =  
885 Red Indian Line; SA = St. Anthony; TP = Tally Pond Belt; TU = Tulks Volcanic Belt;  
886 VA = Victoria Arc; WB = Wild Bight Group.

887

888 Figure 2. Geological map of the Springdale Peninsula with the position of known VMS  
889 deposits within the region (modified from Kean et al., 1995).

890

891 Figure 3. Geological map of the Whalesback and Little Deer area (Modified from  
892 Papezik and Fleming (1967); Fleming (1970) and Kean et al. (1995)).

893

894 Figure 4. Block model of Cu grade of the Whalesback deposit. Also shown are the pierce  
895 points of the drill hole examined during this study.

896

897 Figure 5. Photographs and photomicrographs of representative samples from the Western  
898 lenses and the Eastern lenses. (A) Pyrite-rich sample from the Western lenses. Sample



899 WB-11-103\_172.8m. (B) Reflected light image of a massive pyrite layer from (A). Pyrite  
900 occurs as euhedral to subrounded grains and are associated with minor sphalerite and  
901 chalcopyrite. (C) Pyrrhotite-rich sample from the Eastern lenses. The pyrrhotite-rich zone  
902 is crosscut by chalcopyrite. Sample WB-12-105\_468.35m. (D) Reflected light image of  
903 the pyrrhotite-rich zone from (C). The pyrrhotite-rich zone contains angular to rounded  
904 grains of pyrite and small aggregates of sphalerite and chalcopyrite. (E) Chalcopyrite-rich  
905 sample from the Eastern lenses. Sample WB-12-108\_657.0m. (F) Reflected light image  
906 of the chalcopyrite-rich zone from (E). The chalcopyrite-rich zone contains angular to  
907 rounded grains of pyrite and small aggregates of sphalerite and pyrrhotite.

908  
909 Figure 6. Photographs and photomicrographs of the different non-massive mineralization  
910 types. (A) Disseminated-type mineralization showing isolated chalcopyrite aggregates in  
911 a matrix of silicate minerals. Sample WB-12-108\_653.95m. (B). Reflected light image of  
912 disseminated chalcopyrite in a chlorite-quartz-titanite matrix. Sample WB-12-  
913 108\_653.95m. (C) Same as (B) under cross-polarized light. (D) Veinlet-type  
914 mineralization showing a pyrrhotite veinlet parallel to  $S_2$  schistosity that is crosscut by  
915 later chalcopyrite veinlets at high angle. Sample WB12-109\_520.2m. (E) Reflected light  
916 image of pyrrhotite veinlet crosscut by later chalcopyrite in a chlorite-quartz matrix.  
917 Sample WB12-109\_520.2m. (F) Same as (E) under cross-polarized light. (G) Breccia-  
918 type mineralization showing chalcopyrite brecciating a chlorite-rich matrix. Sample Wb-  
919 12-109\_442.2m. (H) Reflected light image of showing intergrowth of chalcopyrite with  
920 fibrous chlorite. Sample Wb-12-109\_442.2m. (I) Same as (H) under cross-polarized light.  
921 Abbreviations are as follow: Cal = calcite, Ccp = chalcopyrite, Chl = chlorite, Po =

922 pyrrhotite, Qz = quartz, Sp = sphalerite, Ttn = titanite, RL: reflected light and XP: cross-  
923 polar.

924

925 Figure 7. Photographs and photomicrographs of the different massive mineralization  
926 types. (A) Semi-massive-type mineralization showing subrounded pyrite, pyrrhotite and  
927 chalcopyrite crosscutting a subrounded to rounded pyrite and carbonate layer parallel to  
928  $S_2$  foliation. Sample WB-12-104\_391.5m. (B) Reflected light image of semi-massive  
929 sulfides consisting of subrounded to rounded pyrite, pyrrhotite, and chalcopyrite. Also  
930 shown in pyrrhotite and chalcopyrite intergrowth with fibrous chlorite. Sample WB-12-  
931 104\_391.5m. (C) Same as (B) under cross-polarized light. (D) Massive-type pyrrhotite  
932 and chalcopyrite crosscutted by chalcopyrite veinlets. Sample WB-12-108\_670.75m. (E)  
933 Reflected light image of a massive sulfide consisting of a pyrrhotite-rich matrix  
934 overprinted by chalcopyrite, and fragments of chlorite and quartz. Sample WB-12-  
935 108\_670.75m. (F) Same as (E) under cross-polarized light. Abbreviations are as follow:  
936 Cal = calcite, Ccp = chalcopyrite, Chl = chlorite, Po = pyrrhotite, Py = pyrite, Qz =  
937 quartz, RL: reflected light and XP: cross-polar.

938

939 Figure 8. Photomicrographs of Whalesback sulfide deformation textures. (A) Sphalerite  
940 (ductile) with chalcopyrite disease filling fractures in euhedral to subrounded pyrite  
941 (brittle). Sample WB-12-108\_669.8m; (B) Sphalerite with injected arms of pyrrhotite and  
942 chalcopyrite. Sample WB-12-108\_670.4m; (C) Pyrrhotite with subrounded to rounded  
943 clasts of pyrite (brittle) and aggregates of sphalerite and chalcopyrite (ductile). Sample  
944 WB-12-108\_670.4m; and (D) Chalcopyrite with subrounded to rounded clasts of pyrite

945 (brittle) and aggregates of pyrrhotite (ductile) displaced by chalcopyrite. Sample WB-12-  
946 109\_578.6m. Abbreviations are as follow: Ccp = chalcopyrite, Po = pyrrhotite, Py =  
947 pyrite, Sp = sphalerite, RL: reflected light and XP: cross-polar.

948

949 Figure 9. SIMS analysis location and results. (A) Rounded to subrounded pyrite in a  
950 chalcopyrite matrix from a massive sulfide layers within the Western lenses. Sample  
951 WB-11-102\_163.9m. (B) Subrounded pyrite and aggregates of pyrrhotite in a  
952 chalcopyrite matrix from a highly deformed veinlet type sulfide within the Eastern lenses.  
953 Sample WB-12-109\_578.6m (C) Rounded to subrounded fractured pyrite in a  
954 chalcopyrite matrix from breccia-type mineralization from the Eastern lenses. Sample  
955 WB-12-106A\_561.05m. (D) Rounded to subrounded pyrite in a pyrrhotite and  
956 chalcopyrite matrix from a semi-massive sulfide layer within the Eastern lenses.  
957 Pyrrhotite and chalcopyrite are intergrown with fibrous chlorite (in black). Sample WB-  
958 12-104\_391.5m. (E) Rounded to subrounded pyrite and pyrrhotite matrix crosscut by  
959 chalcopyrite piercement veins within a massive sulfide layer from the Eastern lenses.  
960 Sample WB-12-108\_670.75m. (F) Subrounded pyrite grains in a quartz-chlorite matrix  
961 coexisting with a chalcopyrite-rich area within a massive sulfide layer of the Eastern  
962 lenses. Sample WB-12-111\_452.5m. Abbreviations and sample location colors are as  
963 follow: Ccp = chalcopyrite (red circle), Po = pyrrhotite (blue circle) and Py = pyrite  
964 (green circle). RL = Reflected light.

965

966 Figure 10. Notched whisker plots for sulfur isotopic data for chalcopyrite, pyrrhotite and  
967 pyrite. The width of the notches is proportional to the half width (HW = [75th Percentile

968 – 25th Percentile]  $\times 1.57 / [\sqrt{N}]$ , where N is the population size). The central portion of  
969 the notched is the median and is represented by a line across the whisker box. The whiskers  
970 represent the extent of the dataset. Statistically, the chalcopyrite and pyrrhotite represents  
971 one population while the pyrite represents a different population.

972

973 Figure 11. Spatial distribution of  $\delta^{34}\text{S}$  samples within the Whalesback deposit. Also  
974 shown is range in the  $\delta^{34}\text{S}$  values obtained on pyrite and chalcopyrite mineral separates  
975 from the former Whalesback mine (Bachinski, 1977).

976

977 Figure 12. Schematic representation of the evolution of the Whalesback deposit (A-C) at  
978 the deposit scale and (D-F) at the micro-section scale. (A and D) Formation stage. The  
979 Whalesback deposit is deposited near and/or on the seafloor and displays a spatial  
980 zonation of metals with chalcopyrite- and pyrrhotite-rich sulfides at the base and in the  
981 core of the deposit and pyrite-rich sulfides at the top and more distal parts of the deposit.  
982 The chalcopyrite- and pyrrhotite-rich zone contains of euhedral pyrite while the pyrite-  
983 rich zone is composed of euhedral pyrite and sphalerite with minor pyrrhotite and  
984 chalcopyrite. (B and E) Early  $D_2$  deformation stage. The deposit is compressed along the  
985 lateral axis, creating the main  $S_2$  schistosity in the basalt host rock and ductily deforming  
986 and remobilizing sphalerite and pyrrhotite, and rounding the pyrite grains. Chalcopyrite-  
987 rich lenses were aligned parallel to main  $S_2$  schistosity during that stage. (C and F).  
988 Present day disposition of the Whalesback deposit showing a closed and boudinaged  
989 overturned fold configuration. The late stage of deformation ductily remobilized  
990 chalcopyrite and incorporated fragments of ductile pyrrhotite and brittle pyrite,

991 continuing the mechanical rounding of the pyrite grains. Late chalcopyrite veins crosscut  
992 all the previously formed mineral assemblages.

993

994 Figure 13. Metamorphic pressure-temperature diagram with superposed brittle-ductile  
995 behavior boundaries. Mechanical behavior of common base-metal sulfides at the brittle-  
996 ductile transitions at 5% ductile strain before faulting, and at strain rates in the order of  
997  $7.2 \times 10^{-5} \text{ s}^{-1}$  (diagram modified from Marshall and Gilligan, 1987). The general ductile  
998 remobilization sequence at Whalesback is depicted by the arrow and starts in the  
999 sphalerite ductile domain, followed by sphalerite-pyrrhotite ductile domain and ends in  
1000 the sphalerite-pyrrhotite-chalcopyrite ductile domain. This sequence is only possible for  
1001 temperature below 150°C (grey highlighted area). Abbreviations are as follow: Ccp =  
1002 chalcopyrite, Gn = galena, Po = pyrrhotite, Py = pyrite, Sp = sphalerite.

1003

1004 Figure 14.  $\delta^{34}\text{S}$  vs  $\delta^{34}\text{S}$  plots of coexisting sulfide phases: (A) pyrite-chalcopyrite, (B)  
1005 pyrrhotite-chalcopyrite, and (C) pyrite-pyrrhotite. Isotherms were calculated for  
1006 temperatures between 100 to 750°C using the fraction factors of Kajiwara and Krouse  
1007 (1971). Also shown are the isotopic equilibrium temperatures (in italic).

1008

1009 Figure 15. Sulfur isotopic composition for sulfide derived solely from thermochemical  
1010 sulfate reduction of seawater sulfate (TSR) at 250, 300 and 350°C. (A) Chalcopyrite, (B)  
1011 pyrrhotite, and (C) pyrite. Also shown is the range in sulfur isotopic composition of  
1012 sulfide phases observed during this study.

1013

1014 Figure 16. Modeled sulfide isotopic composition of (A) pyrite, (B) pyrrhotite and (C)  
1015 chalcopyrite deposited at 250, 300 and 350°C in relation to the proportion of TSR and  
1016 igneous sulfide required to produce them. The range of TSR proportion required to  
1017 produce the observed sulfide isotopic composition at Whalesback is highlighted in the  
1018 shaded area. Also shown is the range in sulfur isotopic composition of sulfide phases  
1019 observed during this study.  
1020

## **List of Tables**

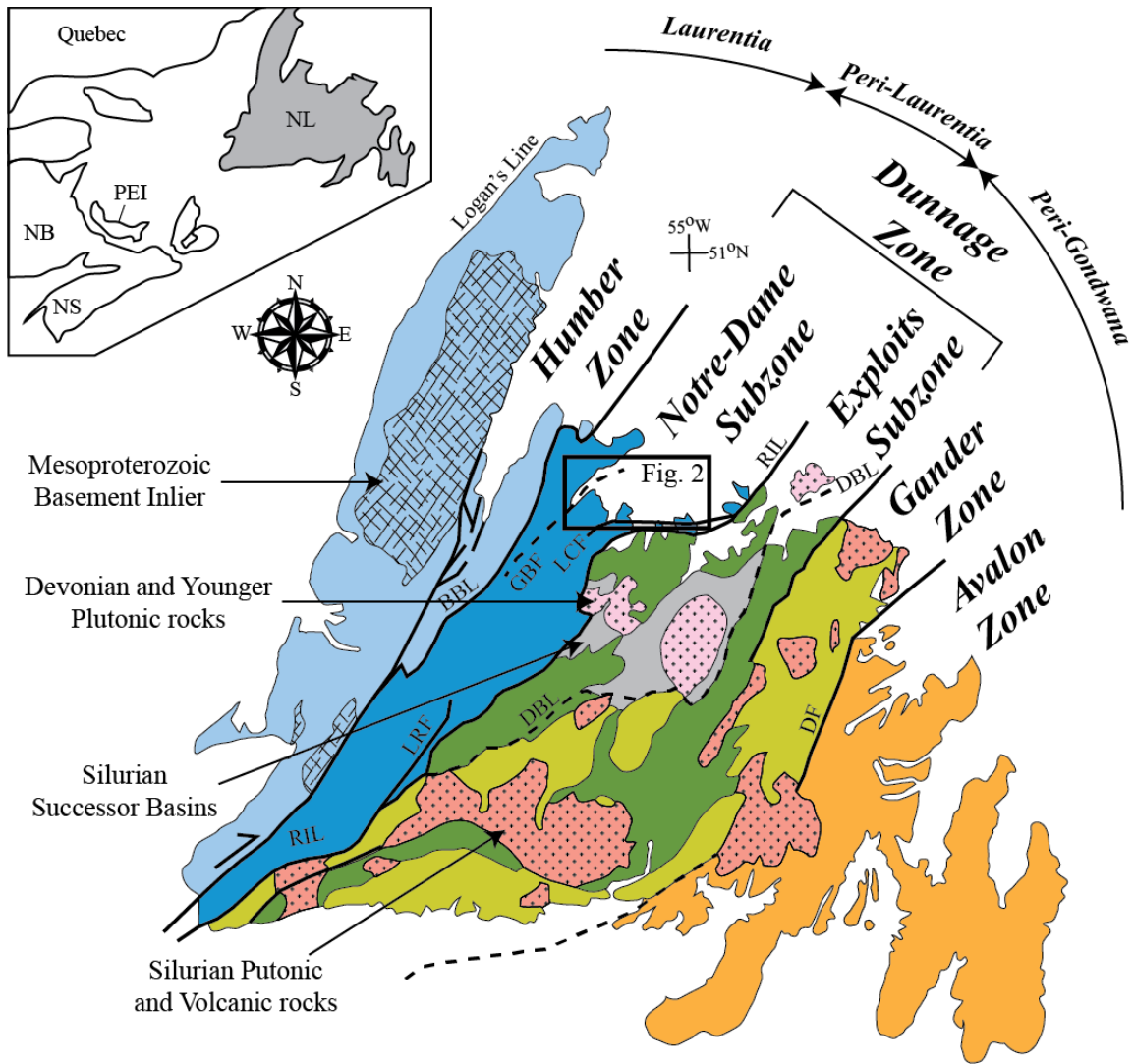
1021

1022

1023 Table 1. SIMS  $\delta^{34}\text{S}$  stable isotopic data for pyrite, pyrrhotite and chalcopyrite phases

1024 from the Whalesback deposit. (See sulfur isotopes section for analytical details).

1025

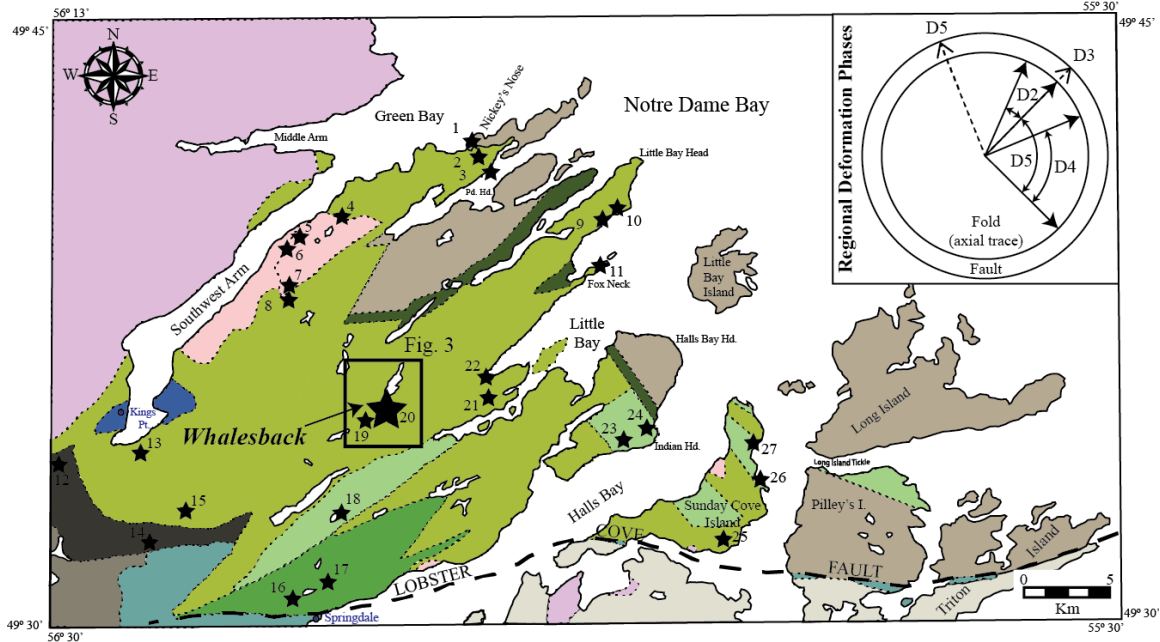


1026

1027 Figure 1

1028





**Legend:**

- Carboniferous**
- Sediments
- Silurian to Devonian**
- Intrusions
- Springdale Group
- Early to Middle Ordovician**
- Robert's Arm Group
- Intrusions
- Western Arm/Cutwell Groups
- Catchers Pond Group
- Undivided mafic tuff and volcanic sediment
- Early Ordovician (and earlier)**
- LUSHS BIGHT GROUP:**
- Pillow Lava (Locally hematized pillow lava with common lenses of jasper)
- Pillow lava (Strongly epidotized)
- Pillow lava (Extensive chlorite schist, highly variolitic with quartz filled amygdules)
- Sheeted diabase dykes

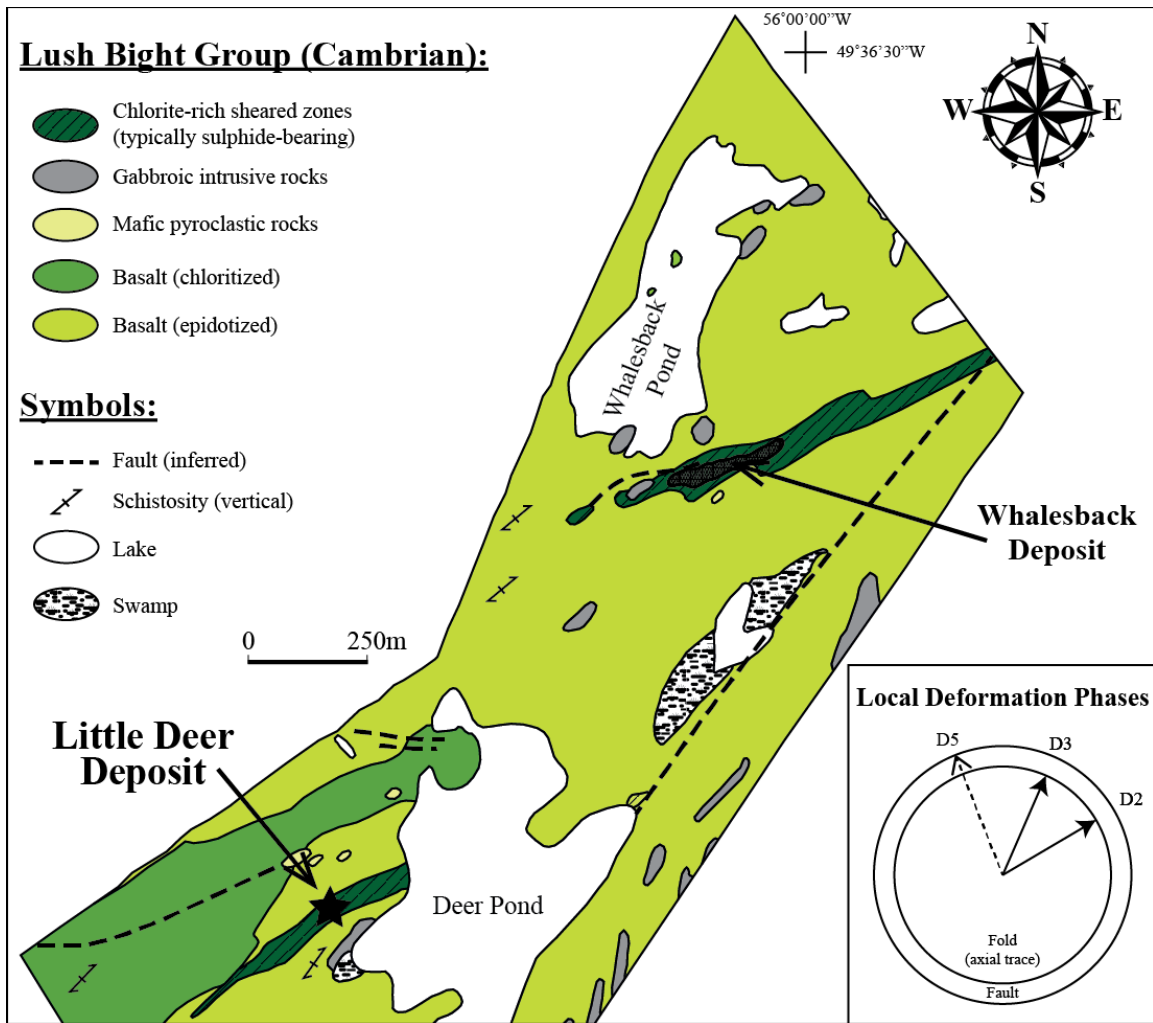
**VMS Occurrences:**

- |   |                                   |
|---|-----------------------------------|
| 1 = Nickey's Nose                       | 14 = Yogi Pond and Nolan          |
| 2 = Rushy Pond                          | 15 = Timber Pond                  |
| 3 = Rushy Pond Head                     | 16 = Sterling                     |
| 4 = Swatridge and Swatridge East        | 17 = Sullivan Pond                |
| 5 = Old English                         | 18 = Lady Pond                    |
| 6 = South Naked Man                     | 19 = Little Deer                  |
| 7 = Colchester and Southwest Colchester | 20 = Whalesback                   |
| 8 = McNeily                             | 21 = Little Bay and Sleepy Hollow |
| 9 = Shoal Arm                           | 22 = Hearn                        |
| 10 = Little Bay Head                    | 23 = Indian Head                  |
| 11 = Fox Neck                           | 24 = Indian Beach                 |
| 12 = Hammer Down                        | 25 = Miles Cove                   |
| 13 = Rendell-Jackman                    | 26 = Jerry Harbour                |
|   | 27 = Paddock Bight                |

1029

1030 Figure 2

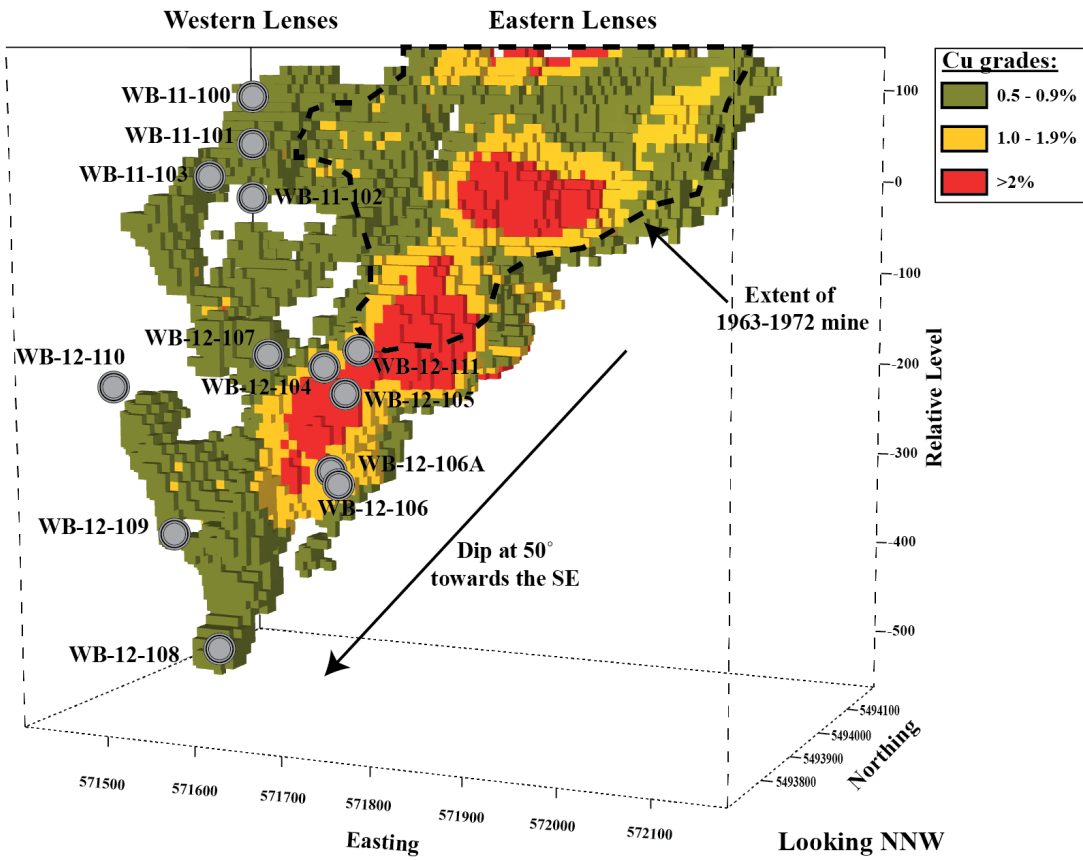
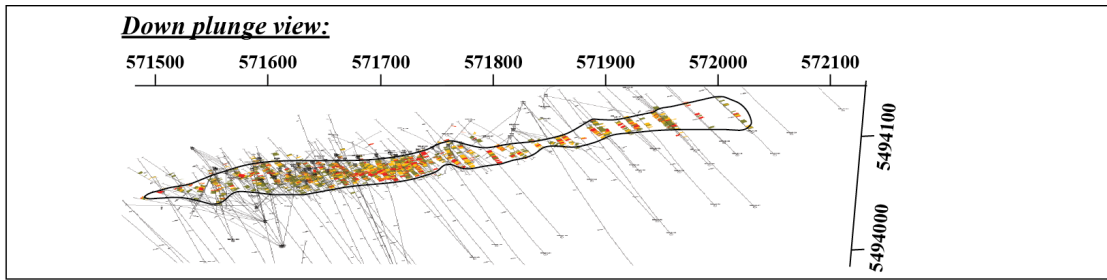
1031



1032

1033 Figure 3

1034



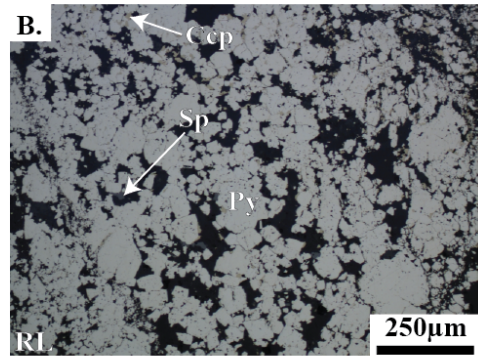
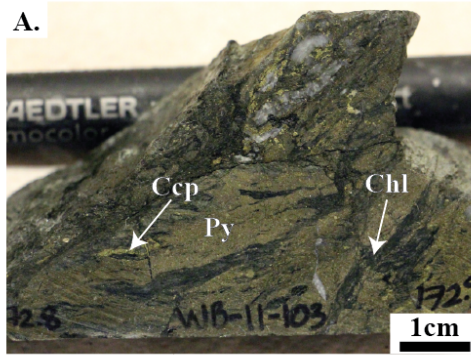
1035

1036 Figure 4

1037

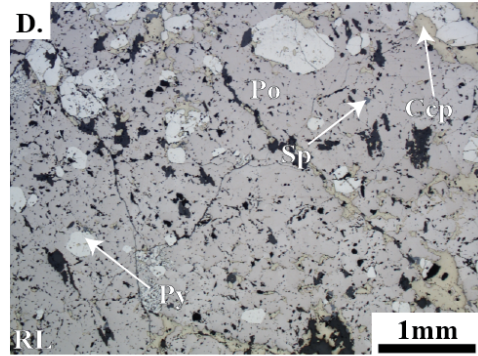
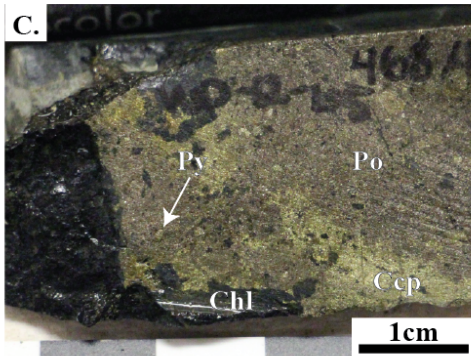
**Western lenses**

**Pyrite-rich**

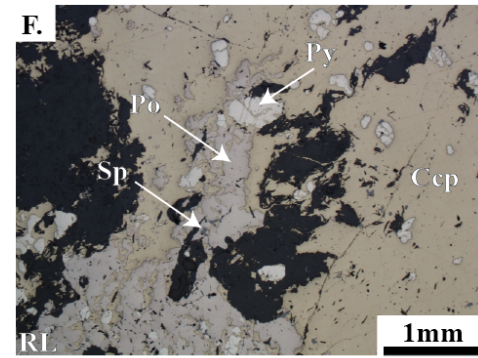
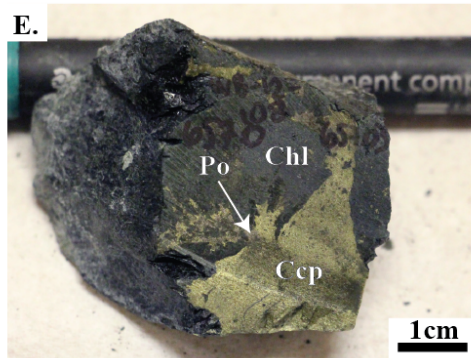


**Eastern lenses**

**Pyrrhotite-rich**



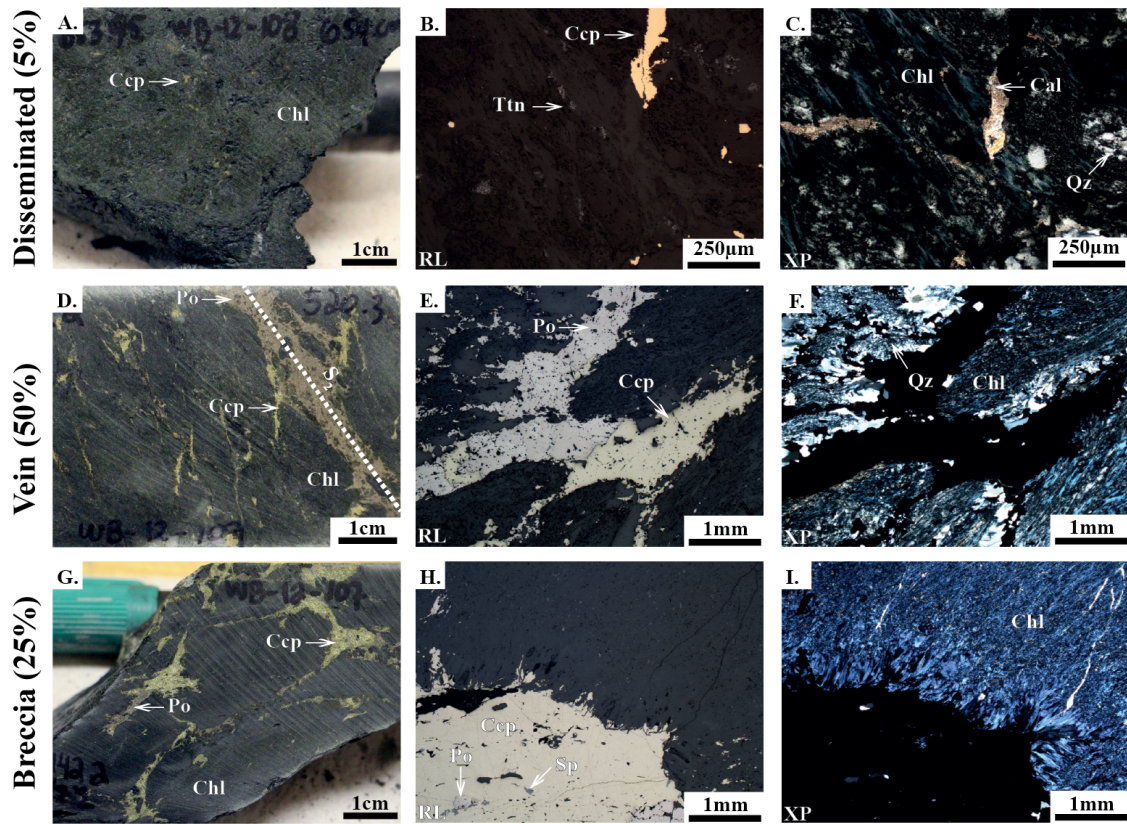
**Chalcopyrite-rich**



1038

1039 Figure 5

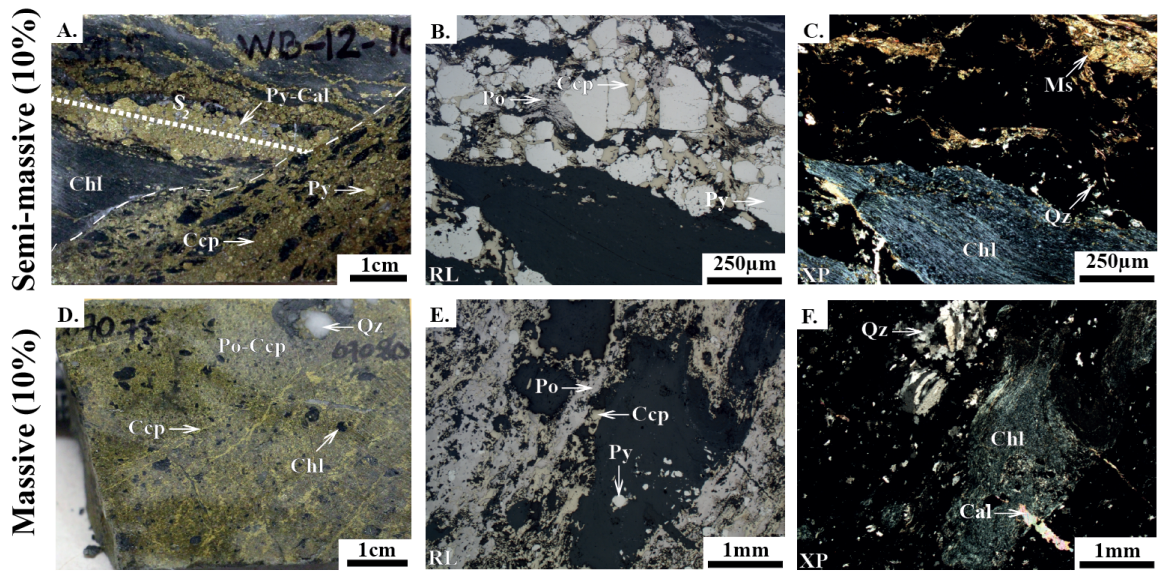
1040



1041

1042 Figure 6

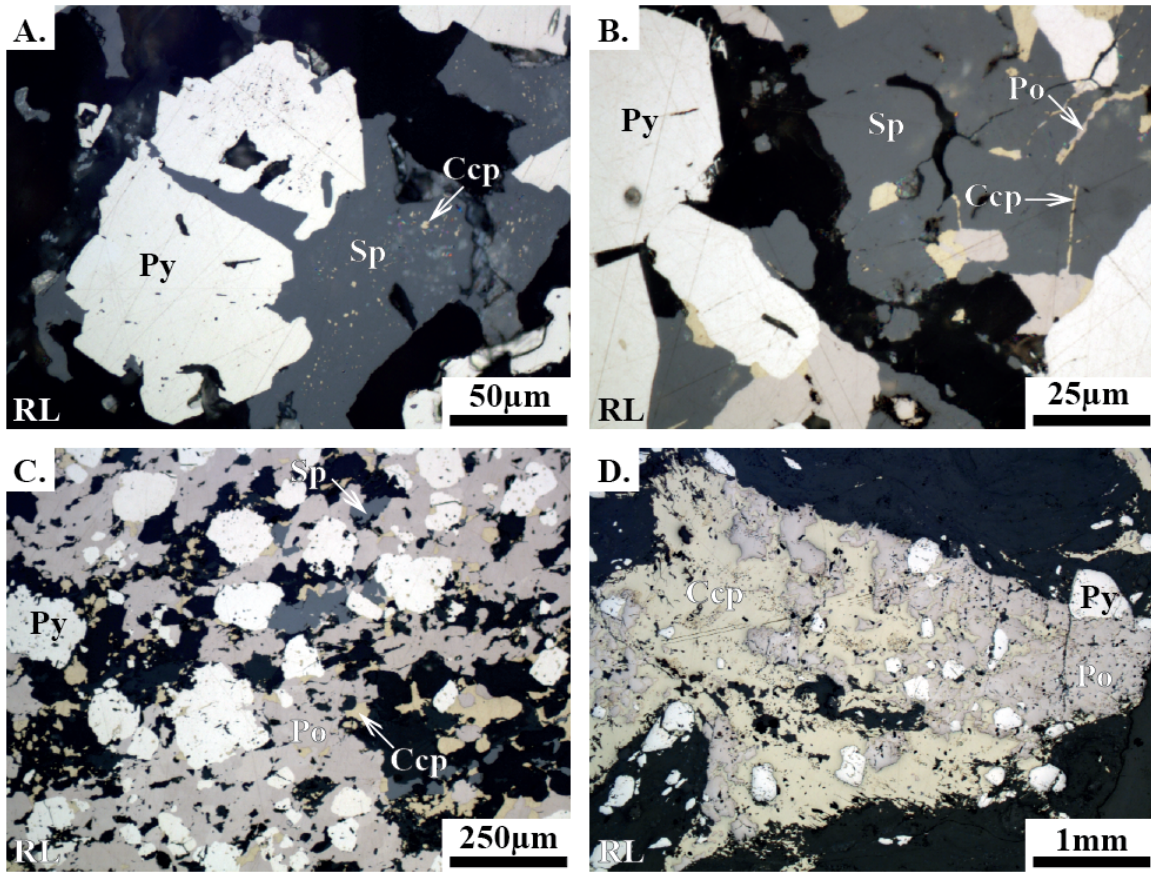
1043



1044

1045 Figure 7

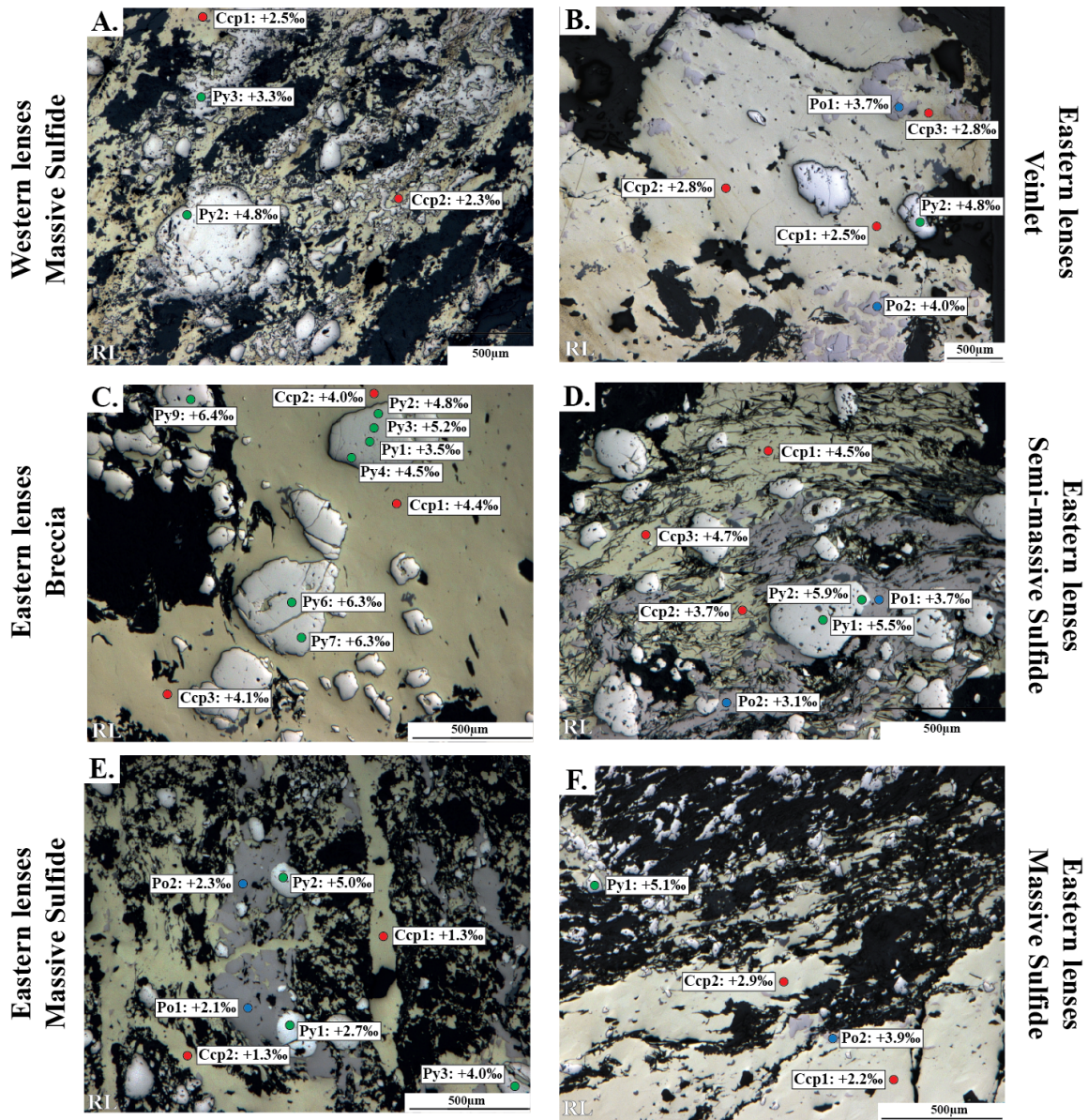
1046



1047

1048 Figure 8

1049

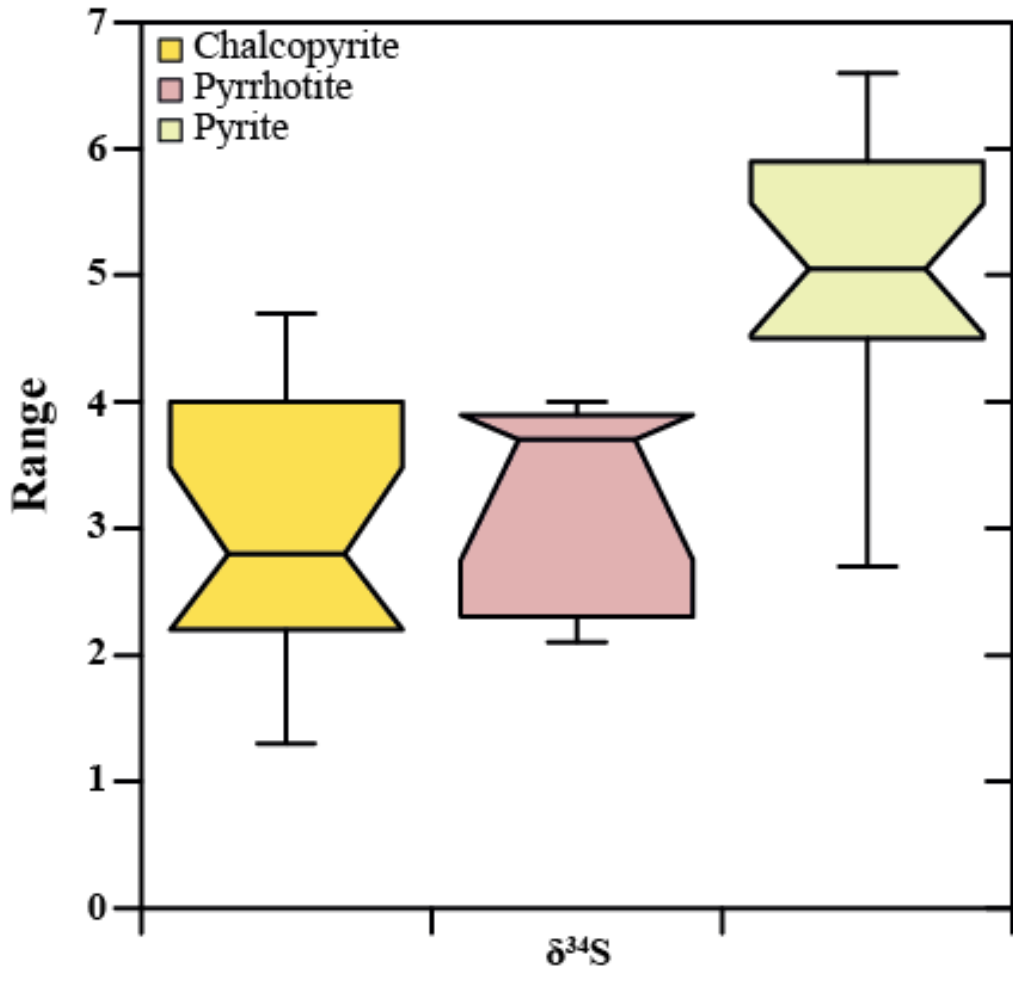


1050

1051 Figure 9

1052

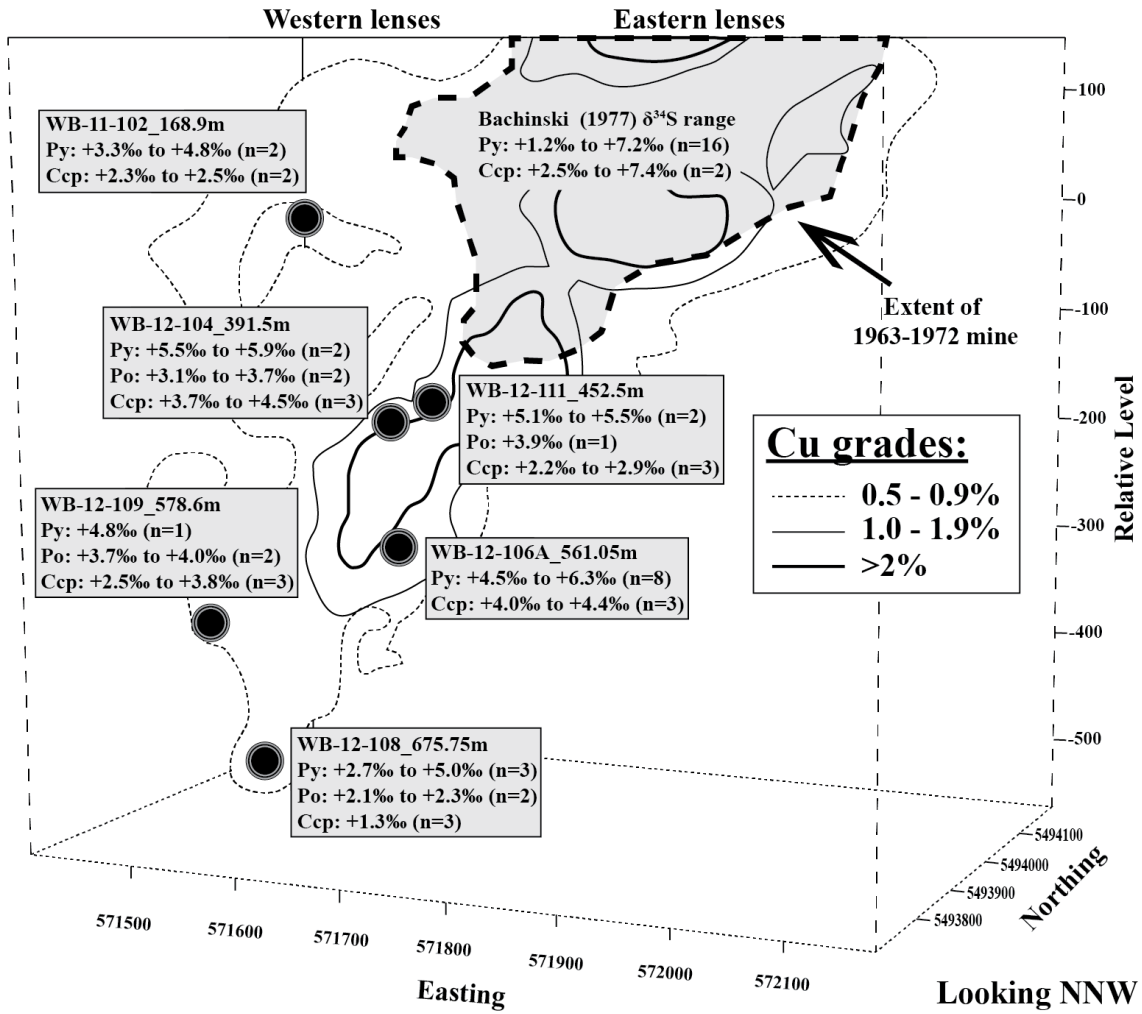




1053

1054 Figure 10

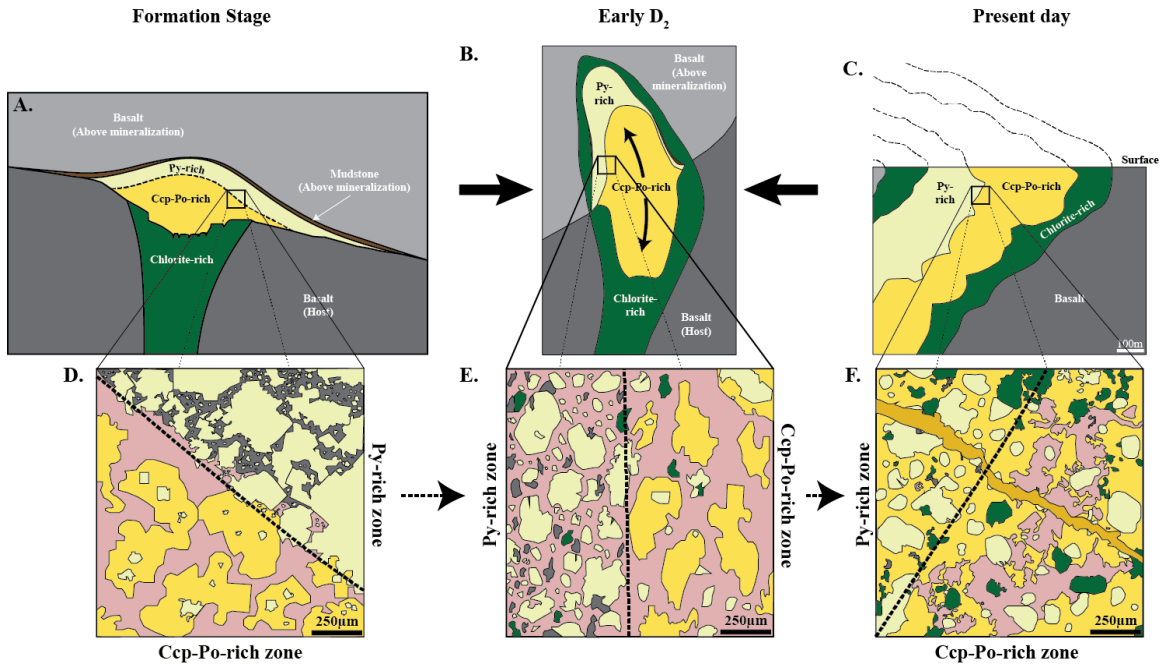
1055



1056

1057 Figure 11

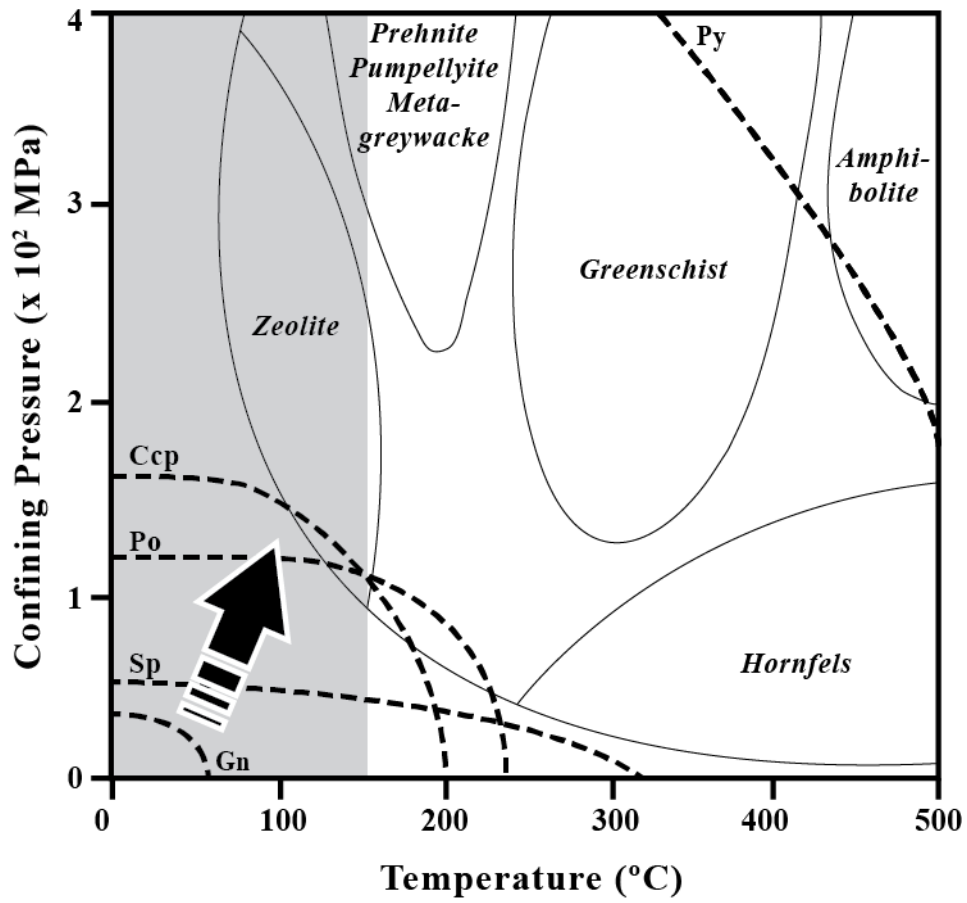
1058



1059 **Legend:** Pyrite Sphalerite Pyrrhotite Chalcopyrite Chalcopyrite (late; vein-type)

1060 Figure 12

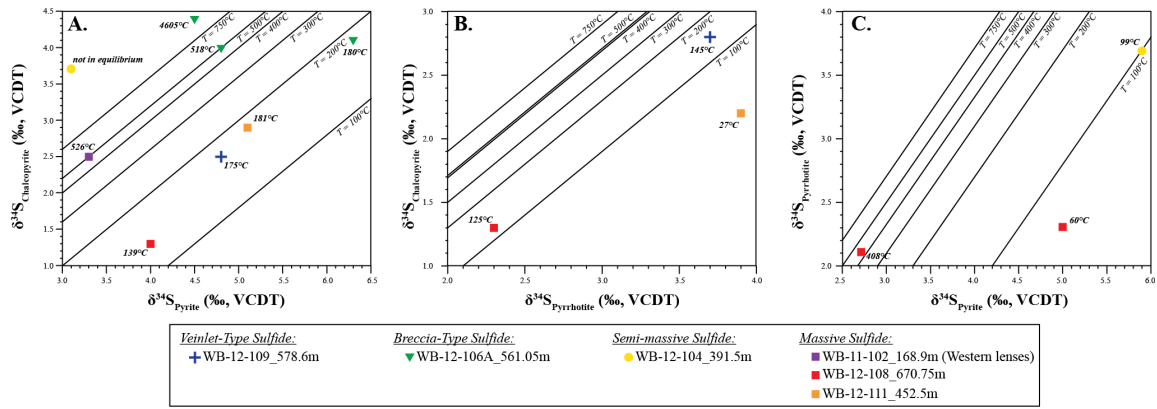
1061



1062

1063 Figure 13

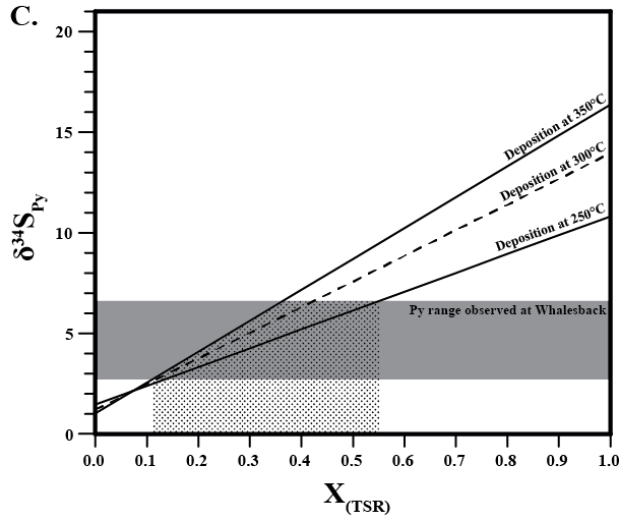
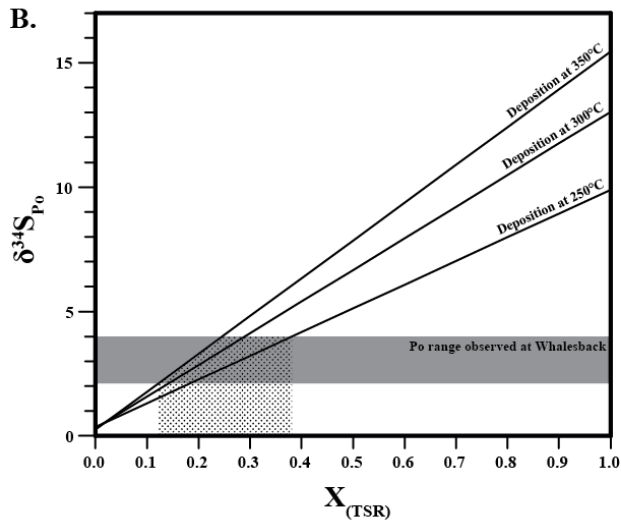
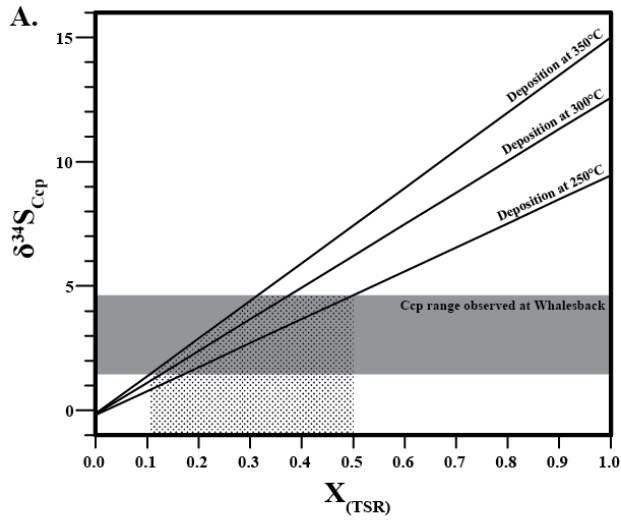
1064



1065

1066 Figure 15

1067



1068

1069 Figure 16

1070

Table 1. SIMS  $\delta^{34}\text{S}$  stable isotopic data for pyrite, pyrrhotite and chalcopyrite phases from the Whalesback deposit. (See sulfur isotopes section for analytical details)

Sample Name	Mineralized Zone	Mineralization Style	$\delta^{34}\text{S}$ (‰)	$1\sigma$
<i>Pyrite:</i>				
WB-11-102_163.9m_Py2	Western lenses	Massive	4.8	0.4
WB-11-102_163.9m_Py3	Western lenses	Massive	3.3	0.3
WB-12-104_391.5m_Py1	Eastern lenses	Semi-Massive	5.5	0.2
WB-12-104_391.5m_Py2	Eastern lenses	Semi-Massive	5.9	0.2
WB-12-106A_561.05m_Py1	Eastern lenses	Breccia	3.5	0.2
WB-12-106A_561.05m_Py2	Eastern lenses	Breccia	4.8	0.2
WB-12-106A_561.05m_Py3	Eastern lenses	Breccia	5.2	0.3
WB-12-106A_561.05m_Py4	Eastern lenses	Breccia	4.5	0.2
WB-12-106A_561.05m_Py6	Eastern lenses	Breccia	6.3	0.3
WB-12-106A_561.05m_Py7	Eastern lenses	Breccia	6.3	0.3
WB-12-106A_561.05m_Py9	Eastern lenses	Breccia	6.4	0.2
WB-12-108_670.75m_Py1	Eastern lenses	Massive	2.7	0.2
WB-12-108_670.75m_Py2	Eastern lenses	Massive	5.0	0.3
WB-12-108_670.75m_Py3	Eastern lenses	Massive	4.0	0.2
WB-12-109_578.6m_Py2	Eastern lenses	Veinlets	4.8	0.3
WB-12-111_452.5m_Py1	Eastern lenses	Massive	5.1	0.2
WB-12-111_452.5m_Py2	Eastern lenses	Massive	5.5	0.2
<i>Pyrrhotite:</i>				
WB-12-104_391.5m_Po1	Eastern lenses	Semi-Massive	3.7	0.3
WB-12-104_391.5m_Po2	Eastern lenses	Semi-Massive	3.1	0.4
WB-12-108_670.75m_Po1	Eastern lenses	Massive	2.3	0.2
WB-12-108_670.75m_Po2	Eastern lenses	Massive	2.1	0.2
WB-12-109_578.6m_Po1	Eastern lenses	Veinlets	3.7	0.2
WB-12-109_578.6m_Po2	Eastern lenses	Veinlets	4.0	0.2
WB-12-111_452.5m_Po2	Eastern lenses	Massive	3.9	0.3
<i>Chalcopyrite:</i>				
WB-11-102_163.9m_Ccp1	Western lenses	Massive	2.5	0.2
WB-11-102_163.9m_Ccp2	Western lenses	Massive	2.3	0.4
WB-12-104_391.5m_Ccp1	Eastern lenses	Semi-Massive	4.5	0.7
WB-12-104_391.5m_Ccp2	Eastern lenses	Semi-Massive	4.7	0.4
WB-12-104_391.5m_Ccp3	Eastern lenses	Semi-Massive	3.7	0.3

1071

1072

Table 1. (continued)

Sample Name	Mineralized Zone	Mineralization Style	$\delta^{34}\text{S}$ (‰)	1 $\sigma$
WB-12-106A-561.05m_Ccp1	Eastern lenses	Breccia	4.4	0.3
WB-12-106A-561.05m_Ccp2	Eastern lenses	Breccia	4.0	0.3
WB-12-106A-561.05m_Ccp3	Eastern lenses	Breccia	4.1	0.3
WB-12-108_670.75m_Ccp1	Eastern lenses	Massive	1.3	0.3
WB-12-108_670.75m_Ccp2	Eastern lenses	Massive	1.3	0.3
WB-12-108_670.75m_Ccp3	Eastern lenses	Massive	1.3	0.3
WB-12-109_578.6m_Ccp1	Eastern lenses	Veinlet	2.5	0.4
WB-12-109_578.6m_Ccp2	Eastern lenses	Veinlet	2.8	0.4
WB-12-109_578.6m_Ccp3	Eastern lenses	Veinlet	2.8	0.3
WB-12-111_452.5m_Ccp1	Eastern lenses	Massive	2.2	0.3
WB-12-111_452.5m_Ccp2	Eastern lenses	Massive	2.9	0.2
WB-12-111_452.5m_Ccp3	Eastern lenses	Massive	2.0	0.6

1073